



# The geochemical fingerprint of microbial long-distance electron transport in the seafloor

Filip J.R. Meysman<sup>a,c,\*</sup>, Nils Risgaard-Petersen<sup>b</sup>, Sairah Y. Malkin<sup>c,1</sup>,  
Lars Peter Nielsen<sup>b</sup>

<sup>a</sup> Department of Ecosystem Studies, The Netherlands Institute of Sea Research (NIOZ), Korrिंगaweg 7, 4401 NT Yerseke, The Netherlands

<sup>b</sup> Section for Microbiology and Center for Geomicrobiology, Department of Bioscience, Aarhus University, 8000 Aarhus C, Denmark

<sup>c</sup> Department of Analytical, Environmental and Geo-Chemistry, Vrije Universiteit Brussel, Pleinlaan 2, 1050 Brussel, Belgium

Received 23 June 2014; accepted in revised form 14 December 2014; Available online 19 December 2014

## Abstract

Recently, a novel “electrogenic” type of sulfur oxidation has been documented in marine sediments, whereby long filamentous cable bacteria are generating electrical currents over centimeter-scale distances. Here we propose a numerical model description that is capable of quantitatively simulating the solute depth profiles and biogeochemical transformations in such electro-active marine sediments. The model is based on a conventional reactive transport description of marine sediments, which is extended with a new model formulation for the long-distance electron transport induced by the cable bacteria. The mechanism of electron hopping is implemented to describe the electron transport along the longitudinal axis of the microbial filaments. We demonstrate that this model is capable of reproducing the observed geochemical fingerprint of electrogenic sulfur oxidation, which consists of a characteristic set of O<sub>2</sub>, pH and H<sub>2</sub>S depth profiles. Our simulation results suggest that the cable bacteria must have a high affinity for both oxygen and sulfide, and that intensive cryptic sulfur cycling takes place within the suboxic zone. A sensitivity analysis shows how electrogenic sulfur oxidation strongly impacts the biogeochemical cycling of sulfur, iron, carbon and calcium in marine sediments.

© 2014 The Authors. Published by Elsevier Ltd. This is an open access article under the CC BY-NC-ND license (<http://creativecommons.org/licenses/by-nc-nd/4.0/>).

## 1. INTRODUCTION

Recently, an entirely novel type of microbial respiration has been discovered, whereby long filamentous bacteria are capable of generating and mediating electrical currents over centimeter-scale distances (Nielsen et al., 2010; Pfeffer et al., 2012; Risgaard-Petersen et al., 2012). This novel “electrogenic” type of microbial sulfur oxidation was first discovered in laboratory experiments (Nielsen et al., 2010), but has recently also been demonstrated to occur under a range of natural conditions, including coastal mud plains, aqua-

culture areas, salt marshes, and seasonally hypoxic basins (Malkin et al., 2014). The process has potentially a large impact on the elemental cycling within the seafloor, as electrogenic sulfur oxidation has been shown to dominate the oxygen consumption, and strongly impacts the cycling of carbon, sulfur and iron with the sediment (Risgaard-Petersen et al., 2012).

The evidence for long distance electron transport is based on electrochemical and geochemical observations in marine sediments. A most remarkable feature of electrogenic sulfur oxidation (e-SOx) is the spatial segregation of redox half reactions, as inferred from O<sub>2</sub>, pH and H<sub>2</sub>S depth profiles (Nielsen et al., 2010). These geochemical data suggest that strong oxidative removal of sulfide takes place in deeper sediment layers, while reductive consumption of oxygen occurs within the oxic zone just below the sediment–water interface (Nielsen et al., 2010). To make such

\* Corresponding author. Tel.: +31 113 577 450.

E-mail address: [filip.meysman@nioz.nl](mailto:filip.meysman@nioz.nl) (F.J.R. Meysman).

<sup>1</sup> Present address: Department of Marine Sciences, University of Georgia, 325 Sanford Dr., Athens GA 30602, USA.

a separation of half-reactions possible, there must be a path by which electrons are transferred from deeper sediment horizons (where electrons are harvested from sulfide) to the surface layer (where electrons are transferred to oxygen). Further support for long-distance electron transfer of electrons was recently obtained by a new type of electrical sediment profiling (Damgaard et al., 2014). When an electron current is induced in the sediment, a corresponding electrical field is anticipated, which drives an ionic counter-current in the pore water to maintain charge balance. Fine-scale measurement of the electric potential distribution in sediments have revealed this predicted electrical field when the geochemical fingerprint of e-SOx is present (Risgaard-Petersen et al., 2014).

Two possible mechanisms were initially proposed to explain the inferred long-distance electron transfer (Nielsen et al., 2010). One possibility is that the conduction occurs within the mineral matrix, where electrons are passed in grain-to-grain contacts between conductive minerals, such as pyrite (Kato et al., 2010; Malvankar et al., 2014). A second option is that the electron transport is microbially mediated (Ntarlagiannis et al., 2007). Microorganisms are known to use diverse strategies such as outer membrane cytochromes, redox shuttles or conductive pili to transport electrons out of the cell and over 1–10  $\mu\text{m}$  distances (Reguera et al., 2005; Gorby et al., 2006; Lovley, 2008; Logan and Rabaey, 2012). However, the inferred electron transport takes place over distances of 10–25 mm (Nielsen et al., 2010; Malkin et al., 2014; Schauer et al., 2014), which exceeds the known length scale of microbial electron transport by more than three orders of magnitude.

Recent investigations provide multiple lines of evidence that long-distance electron transport is microbially mediated. Detailed microscopic investigations have revealed that electro-active sediments contain high densities of unbranched, long filamentous bacteria belonging to the family Desulfobulbaceae, which likely extend from the oxic layer deep into the anoxic zone of the sediment (Pfeffer et al., 2012). When e-SOx is induced in laboratory incubations, the depth distribution of these so-called “cable bacteria” closely tracks the development of the suboxic zone, suggesting that the filaments are responsible for the observed sulfur oxidation (Schauer et al., 2014). Targeted manipulation experiments provide additional support that the cable bacteria are crucially implicated in the electron transport (Pfeffer et al., 2012). A lateral cutting of the filament network (by passing of a thin tungsten wire horizontally through sediment) results in an immediate impediment of the electron transport, as indicated by a sudden and significant drop in the oxygen consumption (Pfeffer et al., 2012). Furthermore, when filters with defined pore sizes were inserted into sediment cores, the downward the downward expansion of electrogenic sulfur oxidation was only observed when the filter barriers had pore sizes that were larger than the diameter ( $\sim 0.5$ – $1 \mu\text{m}$ ) of the filaments (Pfeffer et al., 2012). Finally, when a 5 mm thick layer of non-conductive glass microspheres was inserted into a sediment core, long-distance electron transport was observed when a network of cable bacteria filaments bridged the

non-conductive layer (Pfeffer et al., 2012). These experiments challenge the claim by Malvankar et al. (2014) that currents are passing exclusively through conductive minerals, and instead, support the idea that long-distance electron transfer is mediated by cable bacteria.

Accordingly, the current available observations indicate that an entirely novel mechanism of electron conduction is at work, where electrons are passed on from cell to cell along the longitudinal axis of long, filamentous bacteria (Pfeffer et al., 2012). This finding that microbial activity can facilitate long-distance electron transfer provides a new paradigm for sediment biogeochemistry. The remote spatial coupling of redox half reactions defies conventional ideas of how microbes interact with their environment and how redox cycling occurs within marine deposits (Nealson, 2010). Long-distance electron transfer short-circuits the conventional redox cascade (Froelich et al., 1979) and allows electron acceptors and electron donors to interact with each other without being in close proximity. Moreover, the process substantially reduces the time by which redox oscillations in the water column (e.g., due to changes in  $\text{O}_2$  concentrations) are transduced into deeper sediment layers (Nielsen et al., 2010).

Given its groundbreaking character, the process of electrogenic sulfur oxidation elicits many questions. Are the microbial filaments truly responsible for the electron transport? If so, what is the exact mechanism of electron transfer along a microbial filament? Do we understand the strong pH excursions and other pore water signals observed in electro-active sediments? How strongly does e-SOx affect the elemental cycling in marine sediments? To help answer these questions, a more quantitative underpinning of the current conceptual understanding of e-SOx process is needed. Therefore, the aim of the present study is to develop and apply a biogeochemical model that quantitatively simulates the elemental cycling associated with electrogenic sulfur oxidation. In a first step, we describe the conceptual model of electrogenic sulfur oxidation that has emerged from recent experimental observations. Subsequently, we construct a reactive transport model of an electro-active marine sediment, which includes a mechanistic model of how electrons can be transported along the longitudinal axis of the cable bacteria that perform electrogenic sulfur oxidation. In a third step, we show that this model is capable of quantitatively reproducing the typical biogeochemical fingerprint of e-SOx, as documented by high-resolution  $\text{O}_2$ , pH and  $\text{H}_2\text{S}$  microsensor depth profiling. In a final step, we apply the model to quantitatively evaluate the impact of e-SOx on the biogeochemical cycling of sulfur, iron, carbon and calcium in marine sediments.

## 2. MODEL FORMULATION

### 2.1. Conceptual model of long-distance electron transport

In order to describe sedimentary biogeochemical cycling with mathematical models, one has to make judicious abstractions. Coastal marine sediments are characterized by intense organic matter cycling and a complex sulfur

cycle (Canfield et al., 2005). Oxygen typically disappears within the first few millimeters, due to strong oxygen consumption in the top layer of the sediment (Glud, 2008). In deeper anoxic sediment layers, hydrogen sulfide is generated by dissimilatory sulfate reduction (Jorgensen, 1977), and once produced, this sulfide can have a variety of fates. Part of the sulfide can react with various iron compounds to form iron sulfide phases and eventually pyrite. Another part will be reoxidized to sulfur compounds with intermediate oxidation state (such as elemental sulfur, thiosulfate). Eventually, these intermediates can be converted to sulfate, via a complex interplay of strictly abiotic reactions, as well as microbially catalyzed oxidation and disproportionation reactions (Jorgensen, 1982; Canfield et al., 2005).

For the purpose of this paper, it is useful to consider two idealized pathways of sulfur oxidation (Fig. 1). These two pathways have in common that oxygen features as the electron acceptor, while sulfate acts as the final oxidation product. The principal difference concerns the location of the two half reactions of sulfide oxidation. In the first pathway, referred to as “canonical sulfur oxidation” (abbreviated “c-SOX”), sulfide oxidation and oxygen reduction occur within the same location, i.e., at the oxic–anoxic interface where oxygen ( $O_2$ ) and free sulfide ( $H_2S$ ) are in contact (Fig. 1a). In contrast, the second pathway represents the newly discovered process of “electrogenic sulfur oxidation” (abbreviated “e-SOX”). In this case, long filamentous bacteria are bridging a wide suboxic zone, which separates the oxic and sulfidic sediment horizons (Fig. 1b). The two half-reactions of sulfur oxidation are spatially segregated and are coupled via long-distance electron transport.

As illustrated in Fig. 1, these two sulfur oxidation pathways will each impose a specific “geochemical fingerprint” on the pore water, that is, a characteristic set  $O_2$ , pH, and  $H_2S$  profiles which can be determined by microsensors profiling. In canonical sulfur oxidation, the hydrogen sulfide

produced by sulfate reduction diffuses upwards, and is oxidized to sulfate when it comes into contact with  $O_2$  (Jorgensen and Revsbech, 1983). This reaction is mediated by sulfur oxidizing bacteria, which are positioned at the oxic–anoxic interface. The associated metabolism can be represented by the overall redox reaction:



Electrons are locally transferred between electron donors and acceptors, i.e., across nanometer distances within the membrane-bound enzymes of the electron transport chain (Gray and Winkler, 2005). As a result, no macro-scale electron transport takes place. The associated geochemical fingerprint of canonical sulfur oxidation is characterized by (1) the absence of a suboxic zone, i.e., no separation between the depth at which  $O_2$  disappears and the depth where  $H_2S$  appears, and (2) a decrease of the pH in the oxic zone down to the oxic–anoxic interface, where the oxidation of sulfide releases protons ( $H^+$ ). In deeper anoxic layers, the pH tends to become constant with depth (sulfate reduction releases dissolved inorganic carbon and alkalinity in equal proportions).

Electrogenic sulfur oxidation generates a set of pH,  $O_2$  and  $H_2S$  depth profiles that strongly differs from the geochemical fingerprint of canonical sulfur oxidation (Nielsen et al., 2010). The pH depth profile has a clear maximum at the oxic–anoxic transition and a pronounced pH minimum much deeper in the anoxic zone (Fig. 1b). In addition, there is a prominent suboxic zone, separating the depth where  $O_2$  disappears and the depth where  $H_2S$  appears. Laboratory incubations (Nielsen et al., 2010; Pfeffer et al., 2012; Schauer et al., 2014) as well as field observations (Malkin et al., 2014) indicate that this suboxic zone is typically 10–30 mm wide. Nielsen et al. (2010) argued that the only way to explain this specific geochemical fingerprint

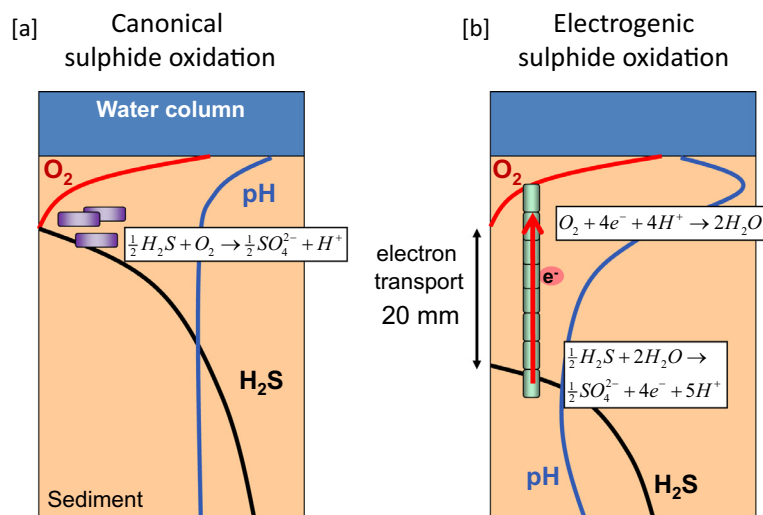
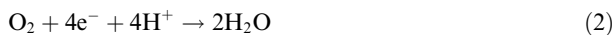
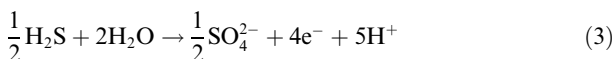


Fig. 1. Conceptual representation of two idealized modes of sulfide oxidation in marine sediments. (a) Canonical sulfur oxidation. The two half reactions occur conjointly at the oxic–anoxic interface. Proton release at the oxic–anoxic interface generates a pH decrease within the oxic zone. (b) Electrogenic sulfur oxidation as proposed by Nielsen et al. (2010). The half-reactions are spatially separated and are linked by electron transport. Strong proton consumption within the oxic zone generates a pH maximum. Deeper down in the sediment, protons are produced due to the oxidation of sulfide, thus creating a pH minimum deeper in the sediment.

is to assume that the two half reactions of sulfide re-oxidation are separated in space. In this conceptual model (Fig. 1b), a cathodic half reaction that involves the  $O_2$  reduction, occurs at the oxic–anoxic interface



The associated consumption of protons generates the observed pH maximum within the oxic zone. At the same time, the anodic half reaction, which involves the  $H_2S$  oxidation, occurs much deeper in the anoxic zone of the sediment



The associated production of protons generates the observed pH minimum deeper in the sediment. The spatial separation of redox half-reactions implies electrical currents running across centimeter scale distances: this electron transport is needed to couple the anodic (i.e., electron producing) half-reaction in the deep anoxic layer with the cathodic (i.e., electron consuming) half-reaction at the oxic–anoxic interface (Fig. 1b).

A full understanding of the geochemical fingerprints associated with the various pathways of sulfur oxidation is crucial for their detection and identification in natural habitats. It was the characterization and interpretation of the distinctive geochemical fingerprint of e-SOx that has led to the original discovery of long-distance electron transport (Nielsen et al., 2010). Similarly, the subsequent observation of this distinct biogeochemical signature in various natural sediments has led to the conclusion that electrogenic sulfur oxidation is a dominant component of the sedimentary sulfur cycle in many marine environments worldwide (Malkin et al., 2014). In the following sections, we will develop a mechanistic model of electrogenic sulfur oxidation, where we translate the conceptual model depicted in Fig. 1 into a reactive transport formulation. This will allow us to compare the geochemical fingerprints of canonical and electrogenic sulfur oxidation.

## 2.2. Reactive transport model

The aim of the biogeochemical model is to simulate the depth profiles of the main pore water solutes and solid sediment constituents in electro-active sediments. In these simulations, we pay special attention to a satisfactory reproduction of the geochemical fingerprint, i.e., the combination of pH,  $O_2$  and  $H_2S$  profiles as determined by micro-sensor profiling. The biogeochemical model has the structure of a conventional early diagenetic model, which is the standard approach to describe reactive transport in marine sediments (Boudreau, 1997; Berg et al., 2003; Meysman et al., 2003). The key innovation is the incorporation of a formulation for the long-distance electron transport associated with electrogenic sulfur oxidation, as described in detail below. The core of the reactive transport model consists of a set of mass balance equations of the form (Boudreau, 1997; Meysman et al., 2005):

$$\phi_F \frac{\partial C_i}{\partial t} = \frac{\partial}{\partial x} \left[ \phi_F D_i \frac{\partial C_i}{\partial x} \right] + \sum_k v_{i,k} R_k \quad (4)$$

The quantity  $C_i$  represents the concentration of a dissolved compound in the pore water, while  $\phi_F$  denotes the porosity (the liquid volume fraction), which is assumed to be constant with depth. For solid components, the mass balance Eq. (4) has an identical form, but the porosity is replaced by the solid volume fraction ( $\phi_S = 1 - \phi_F$ ), while  $C_i$  becomes as the concentration of a solid compound, expressed per unit volume of solid phase.

The transport processes included in the model are tailored to the experimental conditions in which e-SOx develops (Nielsen et al., 2010; Risgaard-Petersen et al., 2012; Schauer et al., 2014) as well as the natural conditions under which the process has been found (Malkin et al., 2014), that is, organic rich coastal sediments, with minimal physical disturbance or bioturbation. The model does not include advective pore water flow, as the sediment is considered cohesive. Bioturbation and bio-irrigation are likewise not included, as macrofaunal reworking of the sediment appears to disrupt the network of filamentous cable bacteria involved in e-SOx (Malkin et al., 2014). Furthermore, the process develops quickly, over a period of days to weeks (Schauer et al., 2014; Malkin et al., 2014), and over this time scale, the influence of sediment deposition and burial can be ignored. As a result, molecular diffusion is the sole dominant transport process for pore water solutes. The molecular diffusion coefficient  $D_i^{mol}$  is first calculated as a function of temperature and salinity using the R package *marelac* (Soetaert et al., 2010) and corrected for tortuosity according to the modified Wiessberg relation of Boudreau (1996b), i.e.,  $D_i = D_i^{mol} / (1 - 2 \ln \phi_F)$ . No diffusive transport is incorporated for solid phase constituents (i.e.,  $D_i = 0$  for solids).

The quantities  $R_k$  in Eq. (4) represent the rates of the biogeochemical reactions, where  $v_{i,k}$  is the stoichiometric coefficient of the  $i$ -th species in the  $k$ -th reaction. The reaction set included in the model is listed in Table 1 and provides a parsimonious description of biogeochemical cycling in organic-rich coastal sediments. The associated kinetic rate expressions are listed in Table 2. The set of kinetic and equilibrium reactions is adopted from existing models of sediment biogeochemistry (Boudreau, 1996a; Van Cappellen and Wang, 1996; Berg et al., 2003; Meysman et al., 2003), to which we have added a new set of reactions to simulate electrogenic sulfur oxidation. Organic matter in the sediment is microbially degraded via aerobic respiration and sulfate reduction (reactions K1 and K2 in Table 1). Sulfate reduction is suppressed under oxic conditions, which is implemented via a conventional limitation-inhibition formulation (Table 2; Soetaert et al., 1996). The free sulfide released by sulfate reduction can be re-oxidized in two different ways, as illustrated in Fig. 1: either via canonical sulfur oxidation (reaction K3 in Table 1) or electrogenic sulfur oxidation (reactions E1 and E2 in Table 1). The rate expression for canonical sulfide re-oxidation follows a standard second-order rate law (Boudreau, 1997; Table 2). The kinetic formulation of electrogenic sulfur oxidation is novel, and is discussed in a separate section below. It is important to note that the relative importance of the two sulfur oxidation pathways is not fixed *a priori*, but forms an emergent property of the model. The rate of each

Table 1

List of biogeochemical reactions included in the sediment model. K-type reactions denotes “Kinetic reactions”, E-type reactions stand for “Electrogenic reactions”, while AB-type reactions correspond to “Acid-base dissociation reactions”.

<i>Kinetic reactions</i>		
K1	Aerobic respiration	$\text{CH}_2\text{O} + \text{O}_2 \rightarrow \text{HCO}_3^- + \text{H}^+$
K2	Sulfate reduction	$\text{CH}_2\text{O} + \frac{1}{2}\text{SO}_4^{2-} \rightarrow \text{HCO}_3^- + \frac{1}{2}\text{HS}^- + \frac{1}{2}\text{H}^+$
K3	Canonical sulfur oxidation	$\frac{1}{2}\text{HS}^- + \text{O}_2 \rightarrow \frac{1}{2}\text{SO}_4^{2-} + \frac{1}{2}\text{H}^+$
K4	Ferrous iron oxidation	$\text{Fe}^{2+} + \frac{1}{4}\text{O}_2 + \frac{3}{2}\text{H}_2\text{O} \rightarrow \text{FeOOH} + 2\text{H}^+$
K5	Carbonate precipitation	$\text{Ca}^{2+} + \text{HCO}_3^- \rightarrow \text{CaCO}_3 + \text{H}^+$
K6	Carbonate dissolution	$\text{CaCO}_3 + \text{H}^+ \rightarrow \text{Ca}^{2+} + \text{HCO}_3^-$
K7	Iron sulfide precipitation	$\text{Fe}^{2+} + \text{HS}^- \rightarrow \text{FeS} + \text{H}^+$
K8	Iron sulfide dissolution	$\text{FeS} + \text{H}^+ \rightarrow \text{Fe}^{2+} + \text{HS}^-$
<i>Electrogenic reactions</i>		
E1	Cathodic oxygen reduction	$\text{O}_2 + 4\text{e}^- + 4\text{H}^+ \rightarrow 2\text{H}_2\text{O}$
E2	Anodic sulfide oxidation	$\frac{1}{2}\text{HS}^- + 2\text{H}_2\text{O} \rightarrow \frac{1}{2}\text{SO}_4^{2-} + 4\text{e}^- + 4.5\text{H}^+$
<i>Acid-base reactions</i>		
AB1	Carbon dioxide dissociation	$\text{CO}_2 + \text{H}_2\text{O} \rightarrow \text{HCO}_3^- + \text{H}^+$
AB2	Bicarbonate dissociation	$\text{HCO}_3^- \rightarrow \text{CO}_3^{2-} + \text{H}^+$
AB3	Borate dissociation	$\text{B}(\text{OH})_3 + \text{H}_2\text{O} \rightarrow \text{B}(\text{OH})_4^- + \text{H}^+$
AB4	Sulfide dissociation	$\text{H}_2\text{S} \rightarrow \text{HS}^- + \text{H}^+$
AB5	Water dissociation	$\text{H}_2\text{O} \rightarrow \text{OH}^- + \text{H}^+$

Table 2

List of kinetic rate expressions for the reactions included in the model. The rate expressions for kinetic reactions K1–K8 are standard formulations used in sediment biogeochemical models (Soetaert et al., 1996; Van Cappellen and Wang, 1996; Boudreau, 1996a,b; Meysman et al., 2003). The rate expressions for electrochemical half-reactions E1 and E2 are newly introduced here (see text for details).

	Reaction	Kinetic rate expression
K1	Aerobic respiration	$R = (1 - \phi)k_{\text{min}}[\text{CH}_2\text{O}] \frac{[\text{O}_2]}{[\text{O}_2] + K_{\text{O}_2}}$
K2	Sulfate reduction	$R = (1 - \phi)k_{\text{min}}[\text{CH}_2\text{O}] \frac{[\text{SO}_4^{2-}]}{[\text{SO}_4^{2-}] + K_{\text{SO}_4^{2-}}} \frac{K_{\text{O}_2}}{[\text{O}_2] + K_{\text{O}_2}}$
K3	Canonical sulfur oxidation	$R = \phi k_{\text{CSO}}[\text{O}_2][\text{HS}^-]$
K4	Ferrous iron oxidation	$R = \phi k_{\text{FIO}}[\text{Fe}^{2+}][\text{O}_2]$
K5	Carbonate precipitation	$R = (1 - \phi)k_{\text{CP}} \left( \frac{[\text{Ca}^{2+}][\text{CO}_3^{2-}]}{K_{\text{CaCO}_3}^{\text{CP}}} - 1 \right)^{n_{\text{CP}}}$
K6	Carbonate dissolution	$R = (1 - \phi)k_{\text{CD}}[\text{CaCO}_3] \left( 1 - \frac{[\text{Ca}^{2+}][\text{CO}_3^{2-}]}{K_{\text{CaCO}_3}^{\text{CD}}} \right)^{n_{\text{CD}}}$
K7	Iron sulfide precipitation	$R = (1 - \phi)k_{\text{ISP}} \left( \frac{[\text{Fe}^{2+}][\text{HS}^-]}{[\text{H}^+]K_{\text{FeS}}^{\text{ISP}}} - 1 \right)^{n_{\text{ISP}}}$
K8	Iron sulfide dissolution	$R = (1 - \phi)k_{\text{ISD}}[\text{FeS}] \left( 1 - \frac{[\text{Fe}^{2+}][\text{HS}^-]}{[\text{H}^+]K_{\text{FeS}}^{\text{ISD}}} \right)^{n_{\text{ISD}}}$
E1	Cathodic oxygen reduction	$R = \phi k_{\text{COR}}[\text{O}_2]X_T(f_C)^{n_{\text{COR}}}$
E2	Anodic sulfide oxidation	$R = \phi k_{\text{ASO}}[\text{HS}^-]X_T(f_F)^{n_{\text{ASO}}}$

pathway is effectively determined by the availability and spatial distribution of their reagents (e.g., if both  $\text{H}_2\text{S}$  and  $\text{O}_2$  are present at a given location, canonical sulfur oxidation will take place).

The model reaction set does not account for organic matter mineralization via the reduction of iron and manganese (hydr)oxides. Reduction of metal (hydr)oxides is important in marine sediments only when strong metal cycling is sustained by continuous solid phase transport (Aller and Rude, 1988; Canfield et al., 1993; Aller, 2014). For example, in the case of iron cycling, solid iron (hydr)oxides need to be transported downwards, reduced and converted to iron sulfides. To complete the iron cycle, these iron sulfides need to be transported upwards and reoxidized back to iron (hydr)oxides upon contact with oxygen. As noted above, strong reworking of the sediment apparently

disrupts the cable bacteria network (Malkin et al., 2014), and is therefore excluded from the model. In the absence of solid phase transport, dissimilatory iron and manganese reduction will not be important as mineralization pathways.

When electrogenic sulfur oxidation is active, the spatial separation of proton-producing and proton-consuming reactions induces strong pH anomalies in the pore water (Nielsen et al., 2010). This in turn promotes the mobilization of solid mineral phases like iron sulfides (FeS) and carbonates (Risgaard-Petersen et al., 2012). The dissolution of metal sulfides and carbonates acts as a buffer against pH excursions, and so, these reactions are included in the reaction set to be able to simulate the pH depth profile accurately (reactions K6 and K8 in Table 1). Ferrous iron ( $\text{Fe}^{2+}$ ) liberated by FeS dissolution moves upwards, where it is oxidized to iron hydroxide (FeOOH) upon contact with

O<sub>2</sub> (reaction K4 in Table 1), and also diffuses downwards, where it precipitates as FeS (reaction K7 in Table 1). Dissolution and precipitation reactions follow standard kinetic rate laws, where the reaction rate scales with the saturation state of the pore water (Boudreau, 1996a,b; Van Cappellen and Wang, 1996; Meysman et al., 2003).

To describe the pH dynamics in the pore water, the biogeochemical model was equipped with a pH calculation procedure. The modelled set of acid-base dissociation reactions includes the carbonate, borate, sulfide and water equilibria (reactions AB1–AB5, Table 1). The associated total alkalinity is hence defined as:

$$A_T = [\text{HCO}_3^-] + 2[\text{CO}_3^{2-}] + [\text{B}(\text{OH})_4^-] + [\text{HS}^-] + [\text{OH}^-] - [\text{H}^+] \quad (5)$$

The equilibrium constants for the acid-base reactions were calculated as a function of temperature and salinity using AquaEnv, a dedicated R-package for acid-base and CO<sub>2</sub> system calculations (Hofmann et al., 2010). Specifically, for the carbonate equilibria, we used the relationships provided by Millero et al. (2006).

For all pore water constituents, a fixed concentration was imposed as a boundary condition at the sediment–water interface. The concentration values were obtained from measured bottom water conditions at the field site (see below). At the lower boundary, a no flux condition was imposed for all pore water solutes. For the solid phase constituents, a similar no flux boundary condition was imposed at both the upper and lower boundaries of the model domain.

### 2.3. Electron transport model

To simulate the impact of electrogenic sulfur oxidation on sediment geochemistry, we need to embed the associated long-distance transport of electrons into the reactive transport formulation. Perturbation experiments suggest that the electron transport occurs along the longitudinal axis of the cable bacteria (Pfeffer et al., 2012). Microscopy reveals that each bacterial filament consists of a long chain of cells, which can exceed 30 mm in length and can contain up to 20,000 individual cells (Pfeffer et al., 2012; Fig. 2a). This serial connection of cells implies that electrons must somehow be passed on from cell to cell. The actual mechanism of this intercellular electron transport is as yet unclear, but Pfeffer et al. (2012) noticed a remarkable ultrastructure within the outer cell wall of the filaments, with fiber-like structures running along the entire length of the filaments (Fig. 2b). Transmission electron microscopy (TEM) shows that these fibers are embedded within in the continuous periplasmic space and electrically insulated from the external medium by a collective outer membrane (Pfeffer et al., 2012). The hypothesis has been put forward is that these fiber structures acts as “conductive wires” enabling the observed electron transfer (Pfeffer et al., 2012).

Here, we follow the hypothesis that these periplasmic fiber structures are indeed conductive, and we propose a possible mechanism for the electron transport through these fiber structures. Our description of electron transport

is based on the mechanism of multistep electron hopping, which was originally developed to describe electrical conductivity in abiotic polymers containing discrete redox groups (Andrieux and Saveant, 1980; Dalton et al., 1990). In this model, electrons are transferred in a bucket-brigade manner along a one-dimensional array of redox sites. Recently, this electron hopping model has been implemented to describe the charge transport within so-called “microbial nanowires” (Strycharz-Glaven et al., 2011; Polizzi et al., 2012). These nanowires are hair-like, nanometer-wide protein structures, which extend as pili from the cell-wall of dissimilatory metal-reducing bacteria like *Shewanella* and *Geobacter* spp. (Reguera et al., 2005). These nanowires have been shown to be electrically conductive (El-Naggar et al., 2010), and are thought to be implicated in the electron transfer from metal-reducing bacteria to solid electron acceptors, such as metal oxide minerals in natural soils and sediments, and electrode surfaces in microbial fuel cells.

Fig. 2c shows a conceptual model scheme of how electrons could be transported along the longitudinal axis of a cable bacterium. Each filament is surrounded by an outer ring of conductive fibers, which are each considered to be a sequential structure of redox-active enzyme complexes, capable of exchanging electrons with their nearest neighbors (these redox molecules are further referred to as electron carriers). The internal structure of the conductive fibers is currently unknown. However, TEM images by Pfeffer et al. (2012) shows that the diameter  $d$  of a conductive fiber ( $\sim 50$  nm) is considerably larger than those of nanowires ( $\sim 5$  nm), and much larger than the typical diameter of known electron carrying enzyme complexes (e.g.,  $< 0.7$  nm in the multi-heme cytochrome MtrC of *Shewanella*). This suggests that a conductive fiber consists of multiple electron carriers in each cross-sectional plane, rather than constituting a single longitudinal chain of electron carriers. Here, we assume that each filament contains  $N_F$  conductive fibers, while each fiber is considered a long cylinder, fully stacked with electron carriers that are arranged on a rectangular grid separated by a distance  $\delta$ . Hence, a conductive fiber will contain  $N_C = A_F/\delta^2$  electron carriers in each cross-section, where  $A_F$  is the cross-sectional area (Fig. 2c). Such a three-dimensional cylindrical packing of redox sites has the same electron transport behavior as  $N_C$  parallel electron carrier chains, as recently demonstrated by the model simulations of Polizzi et al. (2012) for electron transport in nanowire pili.

Each electron carrier chain is idealized as a one-dimensional sequence of electron carriers (Fig. 2c), which each can bind one electron and which are separated by the distance  $\delta$ . A given electron carrier at the  $i$ -th site along the chain can be in two states: free (carrying no electron, denoted as  $X_i$ ) or charged (carrying an electron, denoted as  $X_i^*$ ).



If we introduce  $n_{CB}(x)$  as the density of cable bacteria filaments at a given depth  $x$  in the sediment (i.e., the number of filaments that crosses a horizontal plane at depth  $x$ , in units per m<sup>2</sup>), then  $X_T = n_{CB}(x)N_F A_F/\delta^3$  becomes the

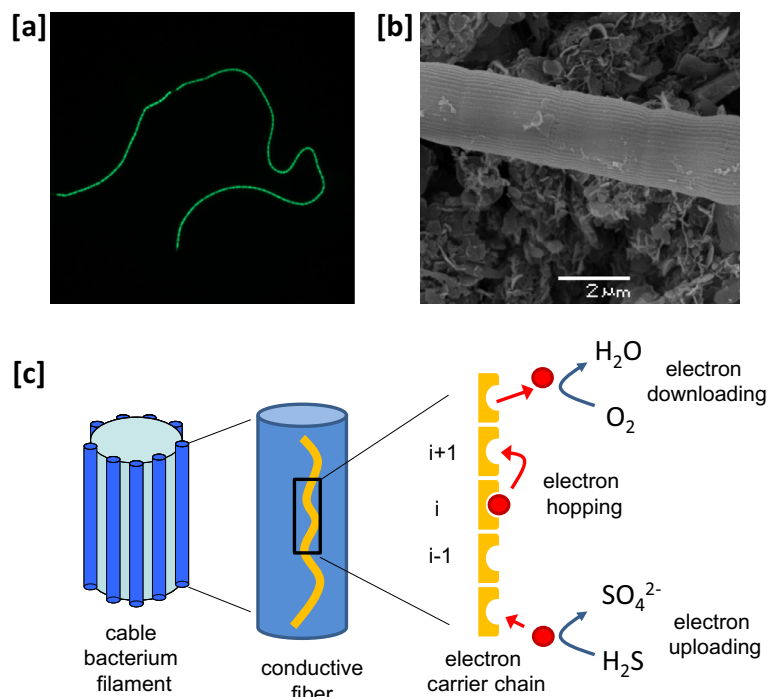
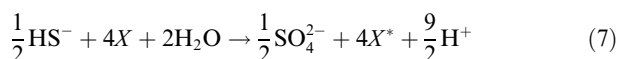


Fig. 2. (a) Microscopic image of a fragment of a cable bacteria filament obtained from the MLG field site and stained by Fluorescent In Situ Hybridisation (see Malkin et al. (2014), for details). The filament consists of a single, unbranched sequence of cells. (b) Scanning Electron Microscopy reveals ridge-like structures running in parallel along the outside of the filaments. These ridges remain continuous across the junction of neighbouring cells and are hypothesized to house the conductive fibers, which are considered the biopolymeric conduits for electron transport. (c) Conceptual model of electron transport in a cable bacterium filament. A single filament is surrounded by conductive fibers in the periplasmic space ( $N_F$  conductive fibers per filament). A single conductive fiber consists out of multiple parallel chains of electron carriers ( $N_C$  chains per fiber). Within each electron carrier chain, electrons are transferred in a bucket-brigade manner along a one-dimensional chain of redox sites.

concentration of electron carriers per unit volume of sediment. The total concentration of charge carriers can be decomposed as  $X_T = [X^*] + [X]$ , where  $[X^*]$  is the concentration of charged electron carriers at a given depth and  $[X]$  is the concentration of free electron carriers. The quantities  $f_C = [X^*]/X_T$  and  $f_F = [X]/X_T$  can be introduced as the fractions charged and free electron carriers respectively.

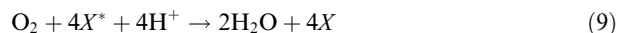
The “uploading” of electrons to the electron transport chain is caused by the oxidation of sulfide within the deeper part of the sediment (Fig. 2c). This can be represented by the reaction equation for anodic sulfide oxidation (ASO):



The associated reaction rate is controlled by the availability of free sulfide, the availability of electron carriers, and the level to which these electron carriers are charged, as reflected by the rate expression:

$$R_{\text{ASO}} = \phi k_{\text{ASO}}[\text{HS}^-]X_T(1 - f_C)^{n_{\text{ASO}}} \quad (8)$$

When all electron carriers are fully charged with electrons ( $f_C \rightarrow 1$ ), the reaction rate vanishes. Similarly, the removal of electrons from the chain occurs via the reduction of oxygen within the oxic zone of the sediment. This is represented by the reaction equation for cathodic oxygen reduction (COR):



The associated kinetic rate expression is given by:

$$R_{\text{COR}} = \phi k_{\text{COR}}[\text{O}_2]X_T(f_C)^{n_{\text{COR}}} \quad (10)$$

Similarly as for anodic sulfide oxidation, this reaction rate is promoted by the availability of the reactants, i.e., oxygen and charged electron carriers. The reaction rate vanishes when charged electron carriers are no longer available ( $f_C \rightarrow 0$ ), and so, electrons cannot be “downloaded” from the electron transport chain.

Next we need to consider the electron transport alongside the electron carrier chains. Electrons will propagate from the anodic part of the electron carrier chain to the cathodic part. By analogy to electron conduction in organic polymers, we assume that electrons can jump from one electron carrier to the next via “electron hopping” (Strycharz-Glaven et al., 2011; Polizzi et al., 2012). This process is described by the bimolecular electron transfer reaction



The hopping frequency  $k$  (units:  $\text{s}^{-1}$ ) is the rate constant of bimolecular electron transfer reaction. Because charge carriers are all identical the forward and backward rate constants are identical. At the macroscale, the hopping of electrons through the carrier network gives rise to an appar-

ent diffusive transport of free and charged electron carriers (Andrieux and Saveant, 1980; Dalton et al., 1990; Strycharz-Glaven et al., 2011; see full derivation in Appendix). The corresponding diffusive fluxes are represented as

$$J_C = -D_E X_T \nabla f_C \quad (12)$$

$$J_F = -D_E X_T \nabla f_F \quad (13)$$

The diffusion coefficient is given by the Dahms–Ruff expression,  $D_E = k\delta^2$ , where  $k$  is hopping frequency and  $\delta$  the distance between charge carriers, as introduced above. This diffusion coefficient  $D_E$  reflects the inherent mobility of electrons through the carrier network. Because the fraction of charged and free carriers must add to unity, i.e.,  $f_F + f_C = 1$ , the diffusive fluxes of charged and free carriers are exactly opposite. This is indeed a necessary consequence of electron hopping: if one charge move upwards, an “empty hole” will move downwards (analogous to the transport of electrons and holes in a semi-conductor).

The flux expressions (12) and (13) for the electron transport within the carrier network, together with the kinetic rate expressions (8) and (10) for the supply and removal of electron on the carrier network, can be implemented in a mass balance equation for the free and charged electron carriers.

$$\phi \frac{\partial [X]}{\partial t} = \frac{\partial}{\partial x} \left[ \phi D_E X_T \frac{\partial f_F}{\partial x} \right] - R_{ASO} + R_{COR} \quad (14)$$

$$\phi \frac{\partial [X^*]}{\partial t} = \frac{\partial}{\partial x} \left[ \phi D_E X_T \frac{\partial f_C}{\partial x} \right] + R_{ASO} - R_{COR} \quad (15)$$

This new submodel for electrogenic sulfur oxidation hence extends the traditional model of sediment biogeochemistry with two new mass balances: one for the free electron carriers  $[X]$  and one for the charged electron carriers  $[X^*]$ . Note that these balance equations are of the diffusion–reaction type, and have the same form as Eq. (4), which is the standard mass balance equation used in sediment biogeochemistry. This implies that we are capable of describing long-distance electron transport within the conventional reactive transport model framework of sediment biogeochemistry. Consequently, the model can be solved with the same numerical methods and techniques that are available for conventional models of sediment biogeochemistry (Boudreau, 1997).

#### 2.4. Numerical solution

Altogether, the model includes 13 state variables: the concentration of organic matter  $[\text{CH}_2\text{O}]$ , oxygen  $[\text{O}_2]$ , sulfate  $[\text{SO}_4^{2-}]$ , ferrous iron  $[\text{Fe}^{2+}]$ , iron sulfides  $[\text{FeS}]$ , total free sulfide  $\Sigma\text{H}_2\text{S} = [\text{H}_2\text{S}] + [\text{HS}^-]$ , total carbonate  $\Sigma\text{CO}_2 = [\text{CO}_2] + [\text{HCO}_3^-] + [\text{CO}_3^{2-}]$ , total borate  $\Sigma\text{B}(\text{OH})_3 = [\text{B}(\text{OH})_3] + [\text{B}(\text{OH})_4^-]$ , alkalinity  $A_T$ , calcium  $[\text{Ca}^{2+}]$ , calcium carbonate  $[\text{CaCO}_3]$ , free electron carriers  $[X]$  and charged electron carriers  $[X^*]$ . A numerical solution procedure for the resulting partial differential equations was implemented in the open-source programming language R, following the procedures of Hofmann et al. (2008) and Soetaert and Meysman (2012). The combination of the mass balance Eq. (4) for each compound together with the mass action laws of the

acid-base equilibria leads to a differential–algebraic system, which was solved using an operator splitting approach (Solution method [3b] as explained in Hofmann et al., 2008). Following the method-of-lines, we used the R-package ReacTran to expand the spatial derivatives of the partial differential equations over the sediment grid using finite differences (see Soetaert and Meysman, 2012 for details). This finite difference grid was obtained by dividing the sediment domain (thickness  $L = 5$  cm) into a grid of 100 sediment layers. After finite differencing, the resulting set of ordinary differential equations was integrated using the stiff equation solver vode from the R-package deSolve (Soetaert et al., 2010).

The calculation of the pH equilibrium at each time step of the numerical simulation was performed via the operator splitting approach as detailed in Hofmann et al. (2008). Numerical integration of the ODE system provides the values of the reaction invariants ( $A_T$ ,  $\Sigma\text{CO}_2$ ,  $\Sigma\text{H}_2\text{S}$ ,  $\Sigma\text{B}(\text{OH})_3$ ) at each time step. Subsequently, the non-linear system of algebraic acid-base expressions was solved for the unknown proton concentration  $[\text{H}^+]$  using the iterative method of Munhoven (2013). Using this proton concentration (or equally pH value), the full speciation could be calculated for all chemical species involved in the acid-base dissociation reactions. The resulting concentrations of the equilibrium species could then be employed in kinetic rate expressions. Specifically, the pore water carbonate ion concentration  $[\text{CO}_3^{2-}]$  was used in the rate expression for calcium carbonate dissolution. The pH values (both data and simulations) are reported on the total pH scale. Further details on this pH model procedure are given in Hofmann et al. (2008).

The electrons within the electron carrier pool have a high turnover rate (i.e., time scale of seconds), due to small size of electron carrier pool and the high rates of electron “uploading” and “downloading” reactions. This fast turnover introduces so-called stiffness into the resulting partial differential equations, which is known to be a challenging problem for numerical integration (Boudreau, 1997). Simulations with a linear dependency ( $n_{COR} = n_{ASO} = 1$ ) in the kinetic expressions (8) and (10) resulted in a poor convergence of the numerical integration routine. Hence, for reasons of numerical stability, we used a quadratic dependency ( $n_{COR} = n_{ASO} = 2$ ) in all further simulations. To test the sensitivity of the model, we performed simulations with a higher order exponent ( $n_{COR} = n_{ASO} = 3$ ). This produced very similar simulation results as a quadratic dependency (differences not distinguishable on graph; results not shown), confirming that the model is not sensitive to the parameters  $n_{COR}$  and  $n_{ASO}$ .

The objective of the model simulations here is to emulate the characteristic biogeochemical fingerprint of e-SOx as observed in laboratory sediment incubations (e.g., Nielsen et al., 2010; Schauer et al., 2014) and field studies (Malkin et al., 2014). One complicating factor in this respect is the apparent transient nature of the phenomenon. In laboratory experiments, whereby e-SOx is induced in homogenized mixtures of natural sediment, the characteristic biogeochemical fingerprint typically emerges after  $\sim 1$  week (Schauer et al., 2014; Malkin et al., 2014). The

sediment subsequently displays a period of intense e-SOx activity, but after ~3–4 weeks, the density and activity of the cable bacteria starts to decline (Schauer et al., 2014). The initial lag period is attributed to biomass build-up within the cable filament network (Schauer et al., 2014), but the details of this development are unclear at present. Similarly, the reasons for the demise of the e-SOx activity after a few weeks are not fully understood, but depletion of the iron sulfide (FeS) pool has been proposed as the likely cause (Schauer et al., 2014). At present, it is unknown whether this successional pattern observed under laboratory conditions is also representative for natural conditions. Currently, field observations of e-SOx activity are only available at isolated time points (Malkin et al., 2014).

The model here does not attempt to fully describe the observed temporal evolution of e-SOx activity. The field dataset used here for model validation (Malkin et al., 2014) shows a similar fingerprint as observed in laboratory incubations after ~3 weeks, when e-SOx rates are highest (Schauer et al., 2014). The primary objective of our model simulations is to reproduce this biogeochemical fingerprint of e-SOx at “peak activity”. To achieve this, we were able to conveniently simplify the model simulation approach.

Firstly, we do not attempt to reproduce the initial lag period, and so, the model does not resolve the biomass dynamics and growth of the filament network. In effect, we assume that at time zero of the simulations, a given filament network is already established. This is done by imposing a given total electron carrier concentration  $E_T$  throughout the sediment. The goal of the simulations is to examine whether and how such a filament network can generate the characteristic geochemical fingerprint.

Secondly, we do not attempt to simulate the observed decline in activity over a time scale of months, and therefore, the model ignores any depletion or accumulation of solid phase constituents. Instead, the concentrations of the three solid phase constituents in the model (organic matter, calcium carbonate, iron sulfides) are kept constant time, which is a reasonable assumption during the short period of peak activity. Large stocks of organic matter, calcium carbonate and iron sulfides are available in the sediment (Table 3), which will only deplete over a time scale of months to years. In addition, no depth gradients were imposed for the solid phase constituents, which mimics the homogenized sediment that is typically used as starting material in laboratory experiments (Nielsen et al., 2010;

Table 3

List of parameters included in the model. Solid phase concentrations are expressed per unit volume of solid phase. The concentration of charge carriers  $E_T$  is expressed per bulk volume of sediment. “Method” refers to the procedure by which parameter values are constrained: A = Measurements, B = Literature values, C = Sensitivity analysis, D = Microscopy data, E = Model Fitting. References: [1] Malkin et al. (2014); [2] Unpublished data from MLG field site; [3] Soetaert et al. (1996); [4] Boudreau (1997); [5] Meysman et al. (2003); [6] Van Cappellen and Wang (1996); [7] Rickard (2006).

	Symbol	Value	Units	Method	References
<i>Environmental parameters</i>					
Temperature	$T$	10	°C	A	[1]
Salinity	$S$	32	–	A	[1]
Pressure	$P$	3.3	bar	A	[1]
Porosity	$\phi$	0.8	–	A	[1]
Concentration organic matter	[CH <sub>2</sub> O]	550	mol m <sup>-3</sup>	A	[2]
Concentration iron sulfide	[FeS]	100	mol m <sup>-3</sup>	A	[2]
Concentration carbonate	[CaCO <sub>3</sub> ]	1300	mol m <sup>-3</sup>	A	[2]
Depth of sediment domain	$L$	5	cm	–	
<i>Biogeochemical parameters</i>					
Mineralization constant	$k_{\min}$	1	yr <sup>-1</sup>	B	[3], [4]
Canonical sulfur oxidation	$k_{\text{CSO}}$	1e+07	mol <sup>-1</sup> m <sup>3</sup> yr <sup>-1</sup>	B	[5], [6]
Ferrous iron oxidation	$k_{\text{FIO}}$	1e+07	mol <sup>-1</sup> m <sup>3</sup> yr <sup>-1</sup>	B	[5], [6]
CaCO <sub>3</sub> precipitation rate constant	$k_{\text{CP}}$	0	mol m <sup>-3</sup> yr <sup>-1</sup>		
CaCO <sub>3</sub> precipitation exponent	$n_{\text{CP}}$	1	–	B	[5]
CaCO <sub>3</sub> dissolution rate constant	$k_{\text{CD}}$	10	yr <sup>-1</sup>	B	[5]
CaCO <sub>3</sub> dissolution exponent	$n_{\text{CD}}$	4	–	B	[5]
FeS precipitation rate constant	$k_{\text{ISP}}$	1e+4	mol m <sup>-3</sup> yr <sup>-1</sup>	B	[5]
FeS precipitation exponent	$n_{\text{ISP}}$	1	–	B	[5]
FeS dissolution rate constant	$k_{\text{ISD}}$	3	yr <sup>-1</sup>	B	[5]
FeS dissolution exponent	$n_{\text{ISD}}$	1	–	B	[5]
Oxygen saturation constant	$K_{\text{O}_2}$	0.001	mol m <sup>-3</sup>	B	[5]
Sulfate saturation constant	$K_{\text{SO}_4^{2-}}$	0.9	mol m <sup>-3</sup>	B	[5]
Solubility CaCO <sub>3</sub>	$K_{\text{CaCO}_3}^{\text{SP}}$	0.39	(mol m <sup>-3</sup> ) <sup>2</sup>	B	[5]
Solubility FeS	$K_{\text{FeS}}^{\text{SP}}$	3.16	mol m <sup>-3</sup>	B	[7]
<i>Electrogenic parameters</i>					
Cathodic oxygen reduction	$k_{\text{COR}}$	1.4e+8	mol <sup>-1</sup> m <sup>3</sup> yr <sup>-1</sup>	C	This work
Anodic sulfide oxidation	$k_{\text{ASO}}$	1.4e+8	mol <sup>-1</sup> m <sup>3</sup> yr <sup>-1</sup>	C	This work
Concentration charge carriers	$X_T$	0.029	mol m <sup>-3</sup>	D	This work
Diffusion coefficient charges	$D_E$	8.4e+4	cm <sup>2</sup> yr <sup>-1</sup>	E	This work

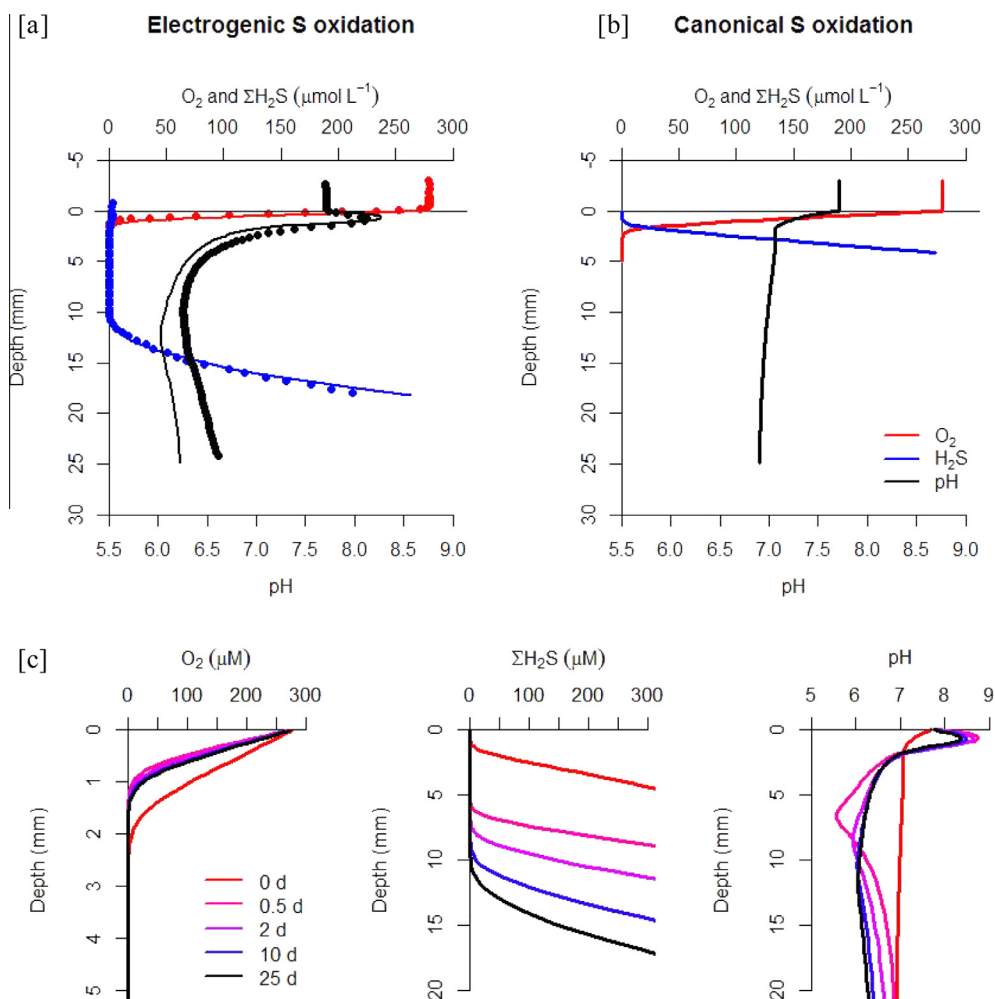


Fig. 3. (a) Electrogenic sulfur oxidation. Comparison between the steady state model simulation (solid lines) and the microsensor field data from Marine Lake Grevelingen (dots). Field data were obtained by microsensor profiles ( $O_2$ , pH,  $H_2S$ ) on sediment cores immediately upon retrieval from the field. The baseline simulation provides the best fit of the model to the data (parameters values listed in Table 3). (b) Steady state model simulation of canonical sulfur oxidation. The model parameter values are exactly the same as in the electrogenic simulation, but for the kinetic rate parameters of the anodic and cathodic half-reactions, which were set to zero ( $k_{ASO} = k_{COR} = 0$ ). (c) Transient model simulation over 25 days showing the transition from canonical sulfur oxidation (initial conditions) to electrogenic sulfur oxidation (final conditions). The depth profiles did not further change after 25 days.

Risgaard-Petersen et al., 2012). The imposed concentration values of the solid phase constituents were derived from solid phase analysis on sediment from the field site (Table 3).

The simulations were dynamically run over a sufficiently long time period (1000 days) so that all pore water concentration profiles attained steady state. Unless stated otherwise, the concentrations of the pore water solutes at all depths were initially set equal to the corresponding values in the overlying bottom water at all depths, apart from oxygen, for which the initial concentration depth profile was set to zero. Again, these initial conditions approximate the starting conditions typically used in the laboratory sediment incubations, i.e., sediment homogenized under an  $N_2$  atmosphere (Risgaard-Petersen et al., 2012). Dynamic simulations starting from different initial conditions arrived at the same steady state (no multiple

stable equilibria). Although the simulated time period was 1000 days in total, we noted that after about 25 days, the solute depth profiles achieved all the main characteristics of the electrogenic fingerprint, and they did not change appreciably any further (Fig. 3c). This time scale closely matches the period of “peak activity” in laboratory incubations, and so, we concur that the simulated steady state concentration profiles are representative for the observed biogeochemical fingerprint of e-SOx at the time of “peak activity”.

## 2.5. Model simulations

The model simulation procedure consisted out of two separate steps. In a first step, a set of the simulations was performed to optimally reproduce the geochemical fingerprint of e-SOx as observed under field conditions.

To this end the steady state model output was compared to a previously published dataset including  $O_2$ , pH and  $H_2S$  microsensor profiles obtained from field measurements in Marine Lake Grevelingen (MLG), a seasonal hypoxic coastal water body in the Dutch Delta area, The Netherlands (see Malkin et al., 2014 for details on sampling site and data collection). The resulting model simulation, which provides the best fit to the given field dataset, is referred to as the “baseline simulation”.

In a second step, we performed a sensitivity analysis, to examine the impact of certain parameters and processes on the biogeochemical cycling within the sediment. To this end, we changed the baseline simulation in three specific ways: (1) inhibition of long-distance electron transport by setting  $k_{COR} = k_{ASO} = 0$  (“No electron transport” simulation), (2) inhibition of iron sulfide dissolution and precipitation by setting  $k_{ISD} = k_{ISP} = 0$  (“No FeS cycling” simulation), and (3) reduction of carbonate buffering by reducing the dissolution rate  $k_{CD}$  by a factor of 4 compared to the baseline simulation (“Reduced  $CaCO_3$ ” simulation).

### 3. RESULTS

#### 3.1. Simulation of the e-SOx biogeochemical fingerprint

Electrogenic sulfur oxidation induces a specific biogeochemical fingerprint upon the pore water, which consists of (1) a shallow oxygen penetration depth, indicative of intense oxygen consumption, (2) a wide suboxic zone that separates the oxic and sulfidic sediment horizons, and (3) strong, characteristic pH excursions (Nielsen et al., 2010; Risgaard-Petersen et al., 2012). Fig. 3a shows a set of  $O_2$ , pH and  $H_2S$  microsensor profiles obtained from field measurements that exhibit this specific biogeochemical fingerprint. At the time of sampling, abundant cable bacteria filaments were detected in these sediments by Fluorescence In Situ Hybridisation (Fig. 2a; Malkin et al., 2014). Fig. 3a additionally shows the simulated  $O_2$ , pH and  $H_2S$  depth profiles from the “baseline simulation”, i.e., the best fit of the model to the dataset. This baseline simulation successfully reproduces the three principal features of the biogeochemical fingerprint: (1) a shallow oxygen penetration, (2) a wide suboxic zone, and (3) the same strong pH excursions as observed in the field data. The fitting procedure and resulting parameter values are discussed in more detail below.

The model simulation shows a similar increase in sulfide concentrations at depth as observed in the field data, and the width of the suboxic zone (operationally defined as difference between the first depth where  $\Sigma H_2S > 5 \mu M$  and the first depth where  $[O_2] < 1 \mu M$ ) is similar in both field data and model simulation (12 mm). Closer examination reveals that the oxygen penetration depth (operationally defined as the depth where  $[O_2] < 1 \mu M$ ) is slightly higher in the baseline simulation (1.7 mm) as compared to the field data (1.2 mm). This suggests that the model slightly underestimates the sedimentary oxygen demand, which is not unexpected, as the model incorporates only a selection of the reoxidation reactions that occur under field conditions (e.g., nitrification is not incorporated).

Yet overall, the baseline simulation reproduces the biogeochemical fingerprint very well. Most importantly, the baseline model is capable of generating very similar pH excursions as seen in the data. Electrogenic sulfur oxidation generates a distinct pH depth profile, which consists of a narrow pH maximum near the oxygen penetration depth (indicative of proton consumption by the cathodic half reaction) followed by a broadly peaked pH minimum in deeper sediment layers (indicative of proton production by the anodic half reaction). This characteristic pH pattern is satisfactorily reproduced by the model. In both model simulation and data, the pH maximum occurs right at the oxygen penetration depth, and is marginally higher in the model (pHmax = 8.27) than in the field data (pHmax = 8.12). A similar broad zone with low pH values stretches across the suboxic zone, where the model slightly overestimates the acidification at depth by 0.22 pH units (pHmin = 6.03 in baseline simulation; pHmin = 6.25 in the field data), indicating that the model presumably lacks a pH buffering mechanism that is present under field conditions.

For comparison, Fig. 3b depicts the output of a model simulation where electrogenic sulfur oxidation has been purposely excluded. To this end, the rate constants of the anodic and cathodic half reactions  $k_{ASO}$  and  $k_{COR}$  were set to zero, while all other parameter values were kept the same as in the electrogenic simulation. The corresponding simulation output shows that e-SOx has a significant impact on the simulated depth profiles. In the absence of e-SOx, no suboxic zone develops (the  $O_2$  and  $H_2S$  profiles show a small overlap), while the oxygen penetration depth is also substantially deeper (2.6 mm). Furthermore, unlike the electrogenic profile in Fig. 3a, the pH depth profile does not generate a subsurface maximum, nor does it show strong acidic conditions at depth (pH decreases within the first 3 mm, and then remains constant around a value of 7). These model simulations with and without e-SOx clearly demonstrate that the typical characteristics of the “electrogenic” fingerprint (shallow  $O_2$  penetration, wide suboxic zone, characteristic pH excursions) are generated by the inclusion of the anodic and cathodic half reactions (E1 and E2 in Table 1).

#### 3.2. The creation of a suboxic zone

The most discriminating features of the “electrogenic” fingerprint are the wide suboxic zone in combination with strong, characteristic pH excursions (Nielsen et al., 2010; Risgaard-Petersen et al., 2012). Note that different interpretations of the term “suboxic zone” are encountered in the literature. In the classical view of sequential redox zonation (Froelich et al., 1979), the suboxic zone is defined as the horizon between the zones of oxygen reduction and sulfate reduction, where other mineralization pathways (nitrate reduction, Mn and Fe reduction) are active. Here, we do not define the suboxic in terms of mineralization pathways, but in terms of pore water concentrations. The suboxic zone is the depth layer where both oxygen and sulfide are undetectably low. As discussed in Section 4.4, sulfate reduction does take place within the suboxic zone, although free

sulfide appears to be absent, thus given rise to cryptic sulfur cycling.

The model presented here provides a mechanistic explanation of how long-distance electron transport can generate the observed suboxic zone. The model simulations reveal how the emergence of the suboxic zone is tightly linked to the dynamics of the electrons within the electron transport network of the cable bacteria. Fig. 4a shows the depth profiles of  $O_2$  and  $H_2S$  in the baseline simulation, alongside the simulated distribution of the charged electron carrier sites  $f_c$  within the sediment. The depth profile of charged carrier sites shows three clear zones: (1) within the oxic zone, electron carriers are not charged ( $f_c \approx 0$ ), (2) within the suboxic zone, electron carriers are partly charged ( $0 < f_c < 1$ ), and (3) within sulfidic zone, electron carriers are completely charged with electrons ( $f_c \approx 1$ ). So at the top of the suboxic zone,  $O_2$  will diffusive downwards until it meets charged electron carriers (so electrons can be “downloaded” from the electron transport network). Conversely, at the bottom of the suboxic zone,  $H_2S$  will start to accumulate as soon as the electron transport network is saturated (all electron carriers are charged and so electrons can no longer be “uploaded” to the electron transport network).

Fig. 4b additionally illustrates this mechanism further by displaying the depth distribution of the reaction rates of cathodic oxygen reduction (COR) and anodic sulfide oxidation (ASO). COR is localized within the oxic zone, and sharply peaks around the oxygen penetration depth (Fig. 4b). In contrast, the ASO is widely distributed across the suboxic zone, and shows a moderate subsurface peak at a depth of 12 mm where  $H_2S$  first appears. This subsurface maximum in ASO is due to the consumption of sulfide diffusing from below, which is generated by sulfate reduction in deeper sediment horizons. Although there is no discernible sulfide within the suboxic zone, the model still shows considerable ASO (Fig. 4b), thus revealing that a strong cryptic sulfur cycle takes place. The sulfide that fuels this

cryptic sulfur cycle is provided by both sulfate reduction as well as FeS dissolution (as further discussed below). Intriguingly, the baseline simulation also indicates that ASO occurs within the oxic zone. As sulfate reduction is prohibited within the oxic zone (Eq. (K2) in Table 2), the sulfide that fuels anodic sulfide oxidation within the oxic zone must be released by FeS dissolution.

### 3.3. Model parameterization

The good correspondence between model simulation and data (Fig. 3a) is encouraging, but one may rightfully question whether this is not the result of a fortuitous choice of model parameters. Hence, a critical issue is to examine how tightly constrained the model is. Stated otherwise, we need to verify whether only one unique set of parameters matches the data, or whether multiple sets of parameter values may provide an equally good fit to the data. To examine this, we devoted substantial effort to a systematic and careful parameterization of the model. This exercise showed that the model parameter set is tightly constrained. Table 3 provides an overview of all parameters, which are classified into three categories, depending on the way that parameters values were constrained. The first category, referred to as “Environmental parameters”, were directly constrained based on the available field data (e.g., temperature, salinity and composition of the overlying bottom water at the field site; porosity, organic carbon, carbonate and iron sulfide composition of the sediment solid phase). The second category, denoted “Biogeochemical parameters”, includes parameters that also feature in conventional models of sediment geochemistry. This includes the parameters in the kinetic rate expressions of organic matter mineralization and subsequent re-oxidation reactions, as well as the parameters describing the dissolution and precipitation of iron sulfide and calcium carbonate. The values of these biogeochemical parameters were constrained based on

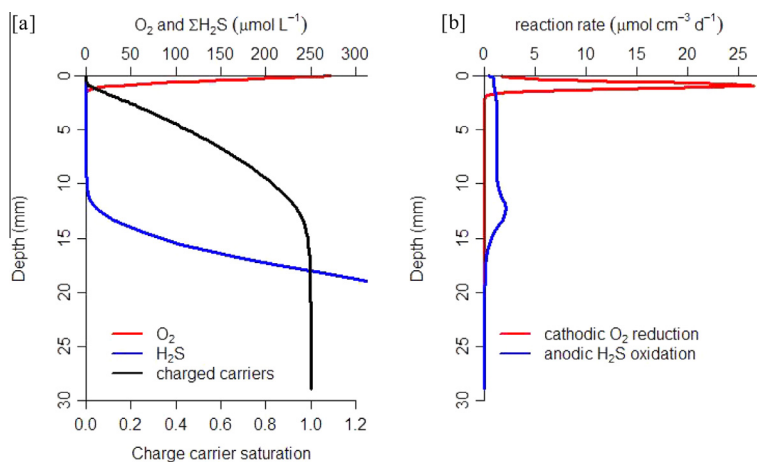


Fig. 4. (a) Simulated depth profiles of  $O_2$  (red line) and  $\Sigma H_2S$  (blue line), together with the simulated depth distribution of charged electron carriers (black solid line). This represents the baseline simulation at steady state (parameters values listed in Table 3) (b) Simulated depth profiles of the reaction rate of the anodic sulfide consumption and cathodic oxygen consumption half-reactions of electrogenic sulfur oxidation. The reaction rates are expressed per unit volume of pore water. (For interpretation of the references to colour in this figure legend, the reader is referred to the web version of this article.)

previous early diagenetic model studies (Table 3 provides the values and references). By including only Environmental and Biogeochemical parameters, one obtains the simulation of canonical sulfur oxidation (as shown in Fig. 3b). The resulting geochemical fingerprint never displays a suboxic zone.

The large difference between the simulation output of canonical sulfur oxidation (Fig. 3b) versus electrogenic sulfur oxidation (Fig. 3a) reveals the strong geochemical effects of e-SOx on sediment biogeochemistry. The e-SOx submodel includes four parameters in total: (1) the density of charge carrier sites  $E_T$  within the electrogenic filament network, (2) the kinetic rate constants  $k_{ASO}$  and  $k_{COR}$  of the anodic and cathodic half reactions, and (3) the charge diffusion coefficient  $D_E$ , which reflects the mobility of charges within the electrogenic filament network. These electrogenic parameters were constrained in a systematic way. In a first step, the value of the charge carrier density  $E_T$  was determined from known information about the morphology of the cable bacteria. Subsequently, the kinetic rate constants  $k_{ASO}$  and  $k_{COR}$  were constrained by a sensitivity analysis. As a result, only one free model parameter remained: the charge diffusion coefficient  $D_E$ . In a final step, the parameter value of  $D_E$  was manually tuned to obtain the best fit to the  $O_2$ ,  $H_2S$  and pH data from the MLG field site. We discuss now this parameterization procedure in more detail.

As already noted above, the density of charge carrier sites  $E_T$  within the filament network can be estimated via the expression  $X_T = n_{CB} N_F A_F / \delta^3$ , and so its value depends on (1) the density  $n_{CB}$  of cable bacteria filaments (expressed per unit of sediment area), (2) the average number of conductive fibers  $N_F$  within the periplasmic space of single bacterial filament, (3) the cross-sectional area  $A_F$  of a single conductive fiber, and (4) the electron carrier interspacing  $\delta$  within the conductive fiber. Although little is known about the structure and geometry of the cable filaments, we tried to constrain each of these four parameters based on available knowledge. At present, there is no direct information on the interspacing  $\delta$  of the electron carriers within the conductive fibers of the filaments. As a first order approach, we hypothesized that the mechanism of electron conduction in conductive fibers could be similar to that in bacterial nanowire pili. Recently, Strycharz-Glaven et al. (2011) estimated a carrier interspacing of  $\sim 1$  nm in bacterial nanowires, based

on the current–voltage data published by El-Naggar et al. (2010). Such an interspacing of  $\delta = 1$  nm is consistent with the heme interspacing in multi-heme cytochromes of *Geobacter* (Pokkuluri et al., 2011) and *Shewanella* (Clarke et al., 2011), and we assumed a similar value here.

Recently, Pfeffer et al. (2012) have reported a filament density  $n_{CB} = 1.2 \times 10^8 \text{ m}^{-2}$  for experimental incubations, while Malkin et al. (2014) reported a similar range  $0.8\text{--}1.2 \times 10^8 \text{ m}^{-2}$  from field observations. There is no specific information on filament density at the MLG field site examined here, but we assume densities are similar, and so we used a filament density  $n_{CB} = 1.2 \times 10^8 \text{ m}^{-2}$  in all simulations. Furthermore, based on scanning electron microscopy, Pfeffer et al. (2012) documented that the number of fibers per filament was  $N_F = 15\text{--}17$ . Malkin et al. (2014) however reported a broader range of  $N_F = 16\text{--}58$  in their field study, presumably reflecting the greater variability in morphology encountered in the different habitats investigated. Here we used the median of the reported range,  $N_F = 36$ . Pfeffer et al. (2012) showed various imagery from transmission electron microscopy, revealing that conductive fibers are approximately 100 nm wide and 40 nm thick, thus providing a value of  $A_F = 4000 \text{ nm}^2$ . By combining the above estimates for all four geometrical parameters, we obtain an electron carrier concentration of  $X_T = 0.029 \text{ mol m}^{-3}$  (expressed per volume of bulk sediment). This was the value for  $X_T$  that we used in all simulations (Table 3).

To determine the values of kinetic rate constants  $k_{ASO}$  and  $k_{COR}$ , we performed a series of auxiliary simulations, starting from the canonical simulation ( $k_{ASO} = k_{COR} = 0$ ), and subsequently, gradually increasing the value of these two kinetic rate constants in tandem, while keeping all other parameters fixed (Fig. 3). Increasing  $k_{ASO}$  and  $k_{COR}$  resulted in a switch from canonical sulfur oxidation to electrogenic sulfur oxidation, and an corresponding expansion of the suboxic zone. However, beyond a given threshold value ( $1.4 \times 10^7 \text{ m}^3 \text{ mol}^{-1} \text{ yr}^{-1}$ ), a further increase of  $k_{ASO}$  and  $k_{COR}$  did no longer change the width of the suboxic zone and the pore water profiles. At this point, free charge carriers are virtually absent from the sulfidic zone, due to the high affinity of the anodic half reaction for free charge carriers (Eq. (8)). Adversely, charged electron carriers immediately vanish whenever  $O_2$  is present, due to the high affinity of the cathodic half reaction. The kinetic rate

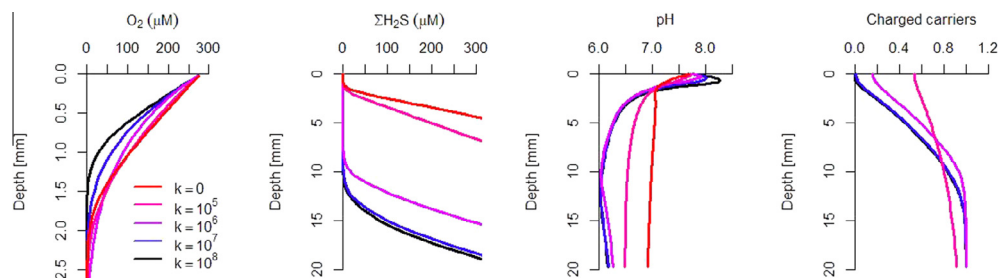


Fig. 5. Sensitivity analysis for the kinetic rate constants of the anodic and cathodic half-reactions ( $k_{ASO} = k_{COR}$  were varied in tandem, represented here as  $k$ ). Steady state depth profiles are plotted. Starting from the canonical simulation ( $k = 0$ ), the value of the two kinetic rate constants were gradually increased, while keeping all other parameters fixed. This results in a transition from canonical sulfur oxidation to electrogenic sulfur oxidation, and an corresponding expansion of the suboxic zone. However, for an increase beyond the threshold value of  $k = 10^8 \text{ mol}^{-1} \text{ m}^3 \text{ yr}^{-1}$  the width of the suboxic zone and the associated the pore water profiles do no longer change.

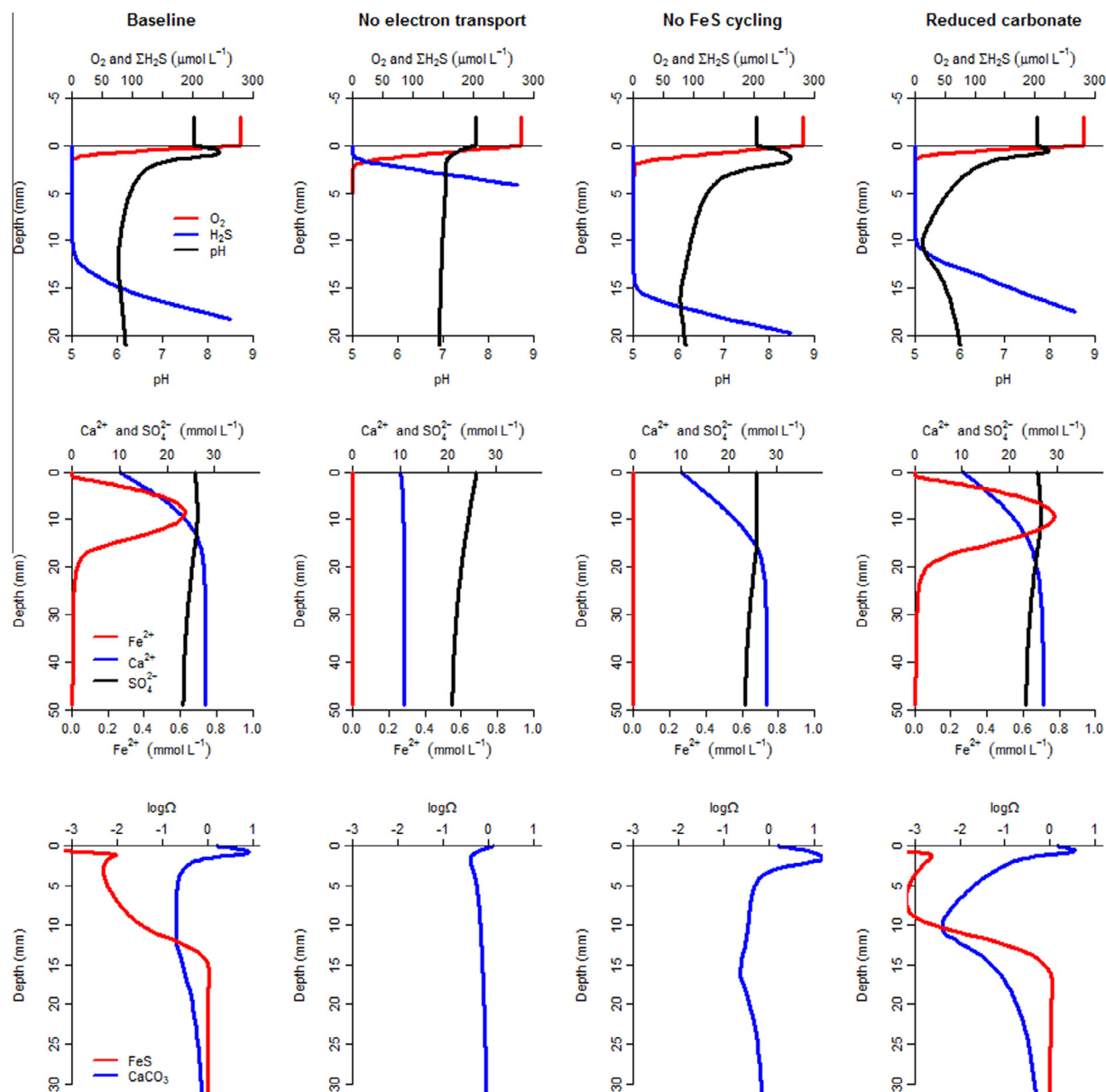


Fig. 6. Comparison of the microsensor fingerprint of different simulations. “Baseline” = Baseline simulation with best fitting parameter set to the field data. “No electron transport” = Simulation with inhibition of long-distance electron transport. “No FeS cycling” = Simulation with inhibition of iron sulfide precipitation and dissolution. “Reduced carbonate” = Simulation with reduced CaCO<sub>3</sub> dissolution. The symbol  $\Omega$  denotes the saturation state of the pore water.

Table 4

Comparison of biogeochemical rates in different model simulations. “Baseline” = baseline simulation. “No e-SOx” = no electrogenic sulfur oxidation. “No FeS” = no iron sulfide precipitation and dissolution. “↓CaCO<sub>3</sub>” = reduced calcium carbonate dissolution.

Process	Unit	Baseline	No e-SOx	No FeS	↓CaCO <sub>3</sub>
Mineralization	mmol C m <sup>-2</sup> d <sup>-1</sup>	13.3	13.2	13.3	13.3
Aerobic respiration	mmol C m <sup>-2</sup> d <sup>-1</sup>	0.4	0.7	0.7	0.4
Sulfate reduction	mmol C m <sup>-2</sup> d <sup>-1</sup>	12.9	12.5	12.6	12.9
Total oxygen uptake	mmol C m <sup>-2</sup> d <sup>-1</sup>	22.7	13.2	13.3	23.6
Cathodic oxygen consumption	mmol O <sub>2</sub> m <sup>-2</sup> d <sup>-1</sup>	21.2	0.0	12.6	22.0
Classical sulfide oxidation	mmol O <sub>2</sub> m <sup>-2</sup> d <sup>-1</sup>	0.1	12.5	0.0	0.1
Ferrous iron oxidation	mmol Fe m <sup>-2</sup> d <sup>-1</sup>	4.2	0.0	0.0	4.6
CaCO <sub>3</sub> dissolution	mmol C m <sup>-2</sup> d <sup>-1</sup>	40.9	3.7	28.8	32.0
Net FeS dissolution	mmol S m <sup>-2</sup> d <sup>-1</sup>	4.2	0.0	0.0	4.6

constants  $k_{\text{ASO}}$  and  $k_{\text{COR}}$  were fixed at these high threshold values (Table 3), reflecting a high affinity of the cable filaments for both  $\text{O}_2$  and  $\text{H}_2\text{S}$ . A biological justification for this could be that natural selection would drive enzymatic efficiencies towards such high affinities. As the auxiliary simulations show, such high affinities are critical for the creation of a suboxic zone, suitably removing  $\text{O}_2$  in the upper layers, and depleting  $\text{H}_2\text{S}$  in deeper layers.

Once the values of  $k_{\text{ASO}}$  and  $k_{\text{COR}}$  are fixed, the sole free parameter in the model is the diffusion coefficient  $D_E$ , which represents the mobility of charges within the filament network. The best model fit to the MLG field data provided  $D_E = 3.5 \times 10^{-7} \text{ m}^2 \text{ s}^{-1}$ . Implementing the Dahms–Ruff expression with an electron carrier interspacing  $\delta = 1 \text{ nm}$ , this provides a hopping frequency  $k = 3.7 \times 10^{12} \text{ s}^{-1}$ . This would make that the electron hopping frequency lies within the picosecond range, which is at the high end of the observed range for electron transport between redox centers in enzymes (Gray and Winkler, 2005).

### 3.4. Sensitivity analysis

Recently, it has been shown that e-SOx can have a large impact on the geochemical cycling within coastal sediments (Risgaard-Petersen et al., 2012). Starting from the baseline simulation, we performed a sensitivity analysis to quantitatively assess how strongly e-SOx affects oxygen consumption, iron sulfide cycling and carbonate dissolution (Simulated depth profiles in Fig. 6; Simulated fluxes in Table 4).

## 4. DISCUSSION

### 4.1. The biogeochemical fingerprint of electrogenic sulfur oxidation

Electrogenic sulfur oxidation provides a novel mechanism to create a suboxic zone in coastal sediments. However, other processes exist in marine sediments that can also create suboxic zones. Large sulfur oxidizing bacteria, like the genus *Beggiatoa*, are able to transport intracellular accumulations of nitrate downward from the sediment surface, and use this nitrate in deeper sediment layers to oxidize  $\text{H}_2\text{S}$  (Sayama et al., 2005). Upon migration upward to the oxic zone, these motile bacteria can utilize oxygen to re-oxidize the elemental sulfur that has accumulated intracellularly. A second way to create a suboxic zone involves sulfide removal through shuttling of iron and manganese (hydr)oxides (Aller and Rude, 1988; Canfield et al., 1993). In this process, metal oxides are transported downwards into the sediment by bioturbation and/or physical mixing, and interact with free sulfide at depth to form metal sulfides (mostly iron sulfides and pyrite). These metal sulfides are then transported upwards again, where they are regenerated near the sediment–water interface upon contact with oxygen.

Neither large sulfur bacteria, nor indications of bioturbation were observed at the MLG field site at the time of sampling (Malkin et al., 2014). Moreover, the presence of the characteristic “electrogenic” pH profile (Fig. 3a)

indicates that e-SOx is responsible for the creation of the suboxic zone at the MLG field site. The defining feature of e-SOx is the spatial separation of redox half reactions, which hence results in a spatial separation of electron production and consumption, thus inducing long-range electrical currents. However, spatial segregation of redox half reactions also implies a spatial separation of proton consumption and proton production, which hence explains the strong pH excursions in the pore water that are observed. The pH maximum near the depth of oxygen penetration is linked to strong proton consumption by cathodic oxygen reduction (Eq. (9)), while the deeper pH minimum is caused by strong proton production due to anodic sulfide oxidation (Eq. (7)).

If the suboxic zone would be created by either large motile bacteria or the shuttling of iron and manganese (hydr)oxides, one would expect to see a very different pH signature. The pH depth profile associated with sulfur oxidation by *Beggiatoa* is characterized by a subsurface pH minimum followed by deeper pH maximum (Sayama et al., 2005). Similarly, when a suboxic zone is created by strong metal cycling, the resulting pH profile also shows a pH minimum at the oxygen penetration depth followed by deeper pH maximum (Jourabchi et al., 2005). Accordingly, these pH profiles show an opposite depth transition (pH min followed by pH max, rather than pH max followed by pH min). Hence, our model simulation results suggest that the observation of the “electrogenic” pH signature can be used as a reliable identifier of electrogenic sulfur oxidation.

As protons are involved in almost any geochemical reaction pathway (Table 1), the pH in natural sediments is influenced by a multitude of biogeochemical processes. As a consequence, an adequate simulation of pH depth profiles in marine sediments is difficult, as models need to select the proper reactions as well as to accurately constrain the rate of these reactions (Meysman et al., 2003; Jourabchi et al., 2005; Soetaert et al., 2007; Hofmann et al., 2008). The fact that we are able to accurately simulate the pH profiles in electro-active sediment of the Grevelingen provides confidence that our baseline simulation captures the principal features of the process of electrogenic sulfur oxidation. As noted above, the reactive transport model forms a direct implementation of the conceptual model of electrogenic sulfur oxidation as displayed in Fig. 1b. Hence, the excellent correspondence between data and simulations quantitatively corroborates the conceptual mechanism of electrogenic sulfur oxidation that has been forwarded (Nielsen et al., 2010; Pfeffer et al., 2012).

### 4.2. Impact on oxygen consumption

Laboratory incubations suggest that electrogenic sulfur oxidation can be a dominant component in the oxygen uptake of coastal sediments (Nielsen et al., 2010; Schauer et al., 2014). Our simulations demonstrate this quantitatively. In the baseline simulation, electrogenic sulfide dominates the overall  $\text{O}_2$  consumption: the cathodic oxygen consumption amounts to  $21.2 \text{ mmol m}^{-2} \text{ d}^{-1}$  and is responsible for the majority (93%) of the total oxygen uptake

(TOU) in the sediment. Canonical sulfur oxidation is negligible as a mode of oxygen consumption ( $0.1 \text{ mmol m}^{-2} \text{ d}^{-1}$  or 0.3%) in the baseline simulation. It is important to emphasize that this absence of canonical sulfur oxidation is not hard-coded into the model, but results from competitive exclusion. Canonical sulfur oxidation requires the presence of both oxygen and free sulfide in the pore water. These conditions are inhibited by electrogenic sulfur oxidation, as long-distance electron transport causes the development of a suboxic zone, which spatially segregates the oxygen and free sulfide horizons. Only when electrogenic sulfur oxidation is purposely excluded (“No electron” simulation, Fig. 6), canonical sulfur oxidation fills in the open niche, and takes over the removal of the free sulfide produced by sulfate reduction.

The TOU in the baseline simulation ( $22.7 \text{ mmol m}^{-2} \text{ d}^{-1}$ ) strongly exceeds the mineralization rate of the sediment ( $13.3 \text{ mmol m}^{-2} \text{ d}^{-1}$  in all simulations). This discrepancy is explained by the dissolution of iron sulfides, which liberates  $\text{H}_2\text{S}$  and  $\text{Fe}^{2+}$ , and hence creates an additional oxygen demand. In the “reduced carbonate” simulation, where more FeS is dissolved (see discussion below), this effect is even more pronounced ( $\text{TOU} = 23.6 \text{ mmol m}^{-2} \text{ d}^{-1}$ ). When the dissolution of the FeS is inactivated (Table 4), the TOU drops and exactly matches the mineralization rate. Since our model implements a 1:1 carbon to  $\text{O}_2$  stoichiometry in organic matter respiration (see reactions K1 and K2 in Table 1), this is also the expected result.

Aerobic mineralization of organic matter only amounts to  $0.5 \text{ mmol m}^{-2} \text{ d}^{-1}$  in the baseline simulation, and hence, it is only responsible for a small part of the TOU in all simulations. The oxygen penetration depth is very small (1.2 mm), and so heterotrophic micro-organisms can only perform aerobic respiration in a thin surface layer, explaining the limited contribution of aerobic mineralization to the TOU. In the baseline simulation, another 4.5% of the TOU is taken up by the oxidation of ferrous iron ( $1.0 \text{ mmol m}^{-2} \text{ d}^{-1}$ ). This ferrous iron is liberated from iron sulfide dissolution as the model does not include dissimilatory iron reduction in the reaction set.

At steady state, the sulfide production will match the sulfide consumption. In turn, the sulfide consumption must match the electron transport, and the electron transport will match the cathodic oxygen consumption. This implies that if the total depth-integrated mineralization rate is fixed, the sulfate reduction will be fixed, and hence, the cathodic oxygen consumption and electron flux will be fixed. As every mole of  $\text{O}_2$  consumed corresponds to the transport of 4 mol of electron, the electrical current densities through the charge carrier network can be calculated as 4 times the cathodic oxygen reduction rate ( $21.2 \text{ mmol m}^{-2} \text{ d}^{-1}$ ). This provides the current density of 85 mmol electrons  $\text{m}^{-2} \text{ d}^{-1}$  in the baseline simulation.

#### 4.3. Iron sulfide dissolution: a respiratory turbo boost

Electrogenic sulfur oxidation requires a source of free sulfide, which acts as the electron donor in deeper anoxic layers. This free sulfide can be supplied in two principal ways (Risgaard-Petersen et al., 2012): either via sulfate

reduction (reaction K2) or via the dissolution of iron sulfides (reaction K8). In the baseline simulation, both pathways are active. Sulfate reduction supplies 60% of the sulfide ( $6.4 \text{ mmol S m}^{-2} \text{ d}^{-1}$ ) while iron sulfide dissolution provides the remaining 40% ( $4.2 \text{ mmol m}^{-2} \text{ d}^{-1}$ ). Hence, cable bacteria performing electrogenic sulfur oxidation obtain a substantial part (40%) of their electron donor supply from previously accumulated FeS minerals. Intriguingly, this dissolution of iron sulfide results from a positive feedback process: electrogenic sulfur oxidation generates acidic conditions within the suboxic zone, which stimulates the dissolution of iron sulfide, which releases free sulfide, which then again stimulates electrogenic sulfur oxidation.

The dissolution of iron sulfide is strongly promoted at lower pH values. In effect, when the pH drops below  $\text{p}K_s = 6.8$  (where  $K_s$  is the first dissociation constant of  $\text{H}_2\text{S}$ ), the saturation state  $\Omega_{\text{FeS}}$  with respect to iron sulfides decreases in a quadratic fashion with the proton concentration (Davison et al., 1999; Rickard, 2006)

$$\Omega_{\text{FeS}} = \frac{[\text{Fe}^{2+}][\text{HS}^-]}{K_{\text{FeS}}^{\text{SP}}[\text{H}^+]} = \frac{[\text{Fe}^{2+}][\text{H}_2\text{S}]}{K_s K_{\text{FeS}}^{\text{SP}}[\text{H}^+]^2} \approx \frac{[\text{Fe}^{2+}]\Sigma\text{H}_2\text{S}}{K_s K_{\text{FeS}}^{\text{SP}}[\text{H}^+]^2} \quad (16)$$

In this expression,  $K_s$  denotes the first dissociation constant of  $\text{H}_2\text{S}$  and  $K_{\text{FeS}}^{\text{SP}}$  is the solubility constant of FeS. At pH values lower than  $\text{p}K_s = 6.8$ , most sulfide is present as  $\text{H}_2\text{S}$ , thus justifying the approximation in Eq. (16). The impact of the pH on iron sulfide dissolution is readily apparent from Fig. 6i, which plots the logarithm of  $\Omega_{\text{FeS}}$  for the baseline simulation. In the suboxic zone, the pore water is acidic and strongly undersaturated, thus driving intense dissolution of FeS. This dissolution leads to a strong accumulation of ferrous iron ( $\text{Fe}^{2+}$ ) in the pore water (Fig. 6). Below the suboxic zone, the pore water becomes oversaturated again, due to a rapid increase in sulfide concentrations with depth. This induces a re-precipitation of iron sulfide at depth, which removes the  $\text{Fe}^{2+}$  that diffuses downwards.

Hence, the protons liberated by electrogenic sulfur oxidation acidify the pore water of the suboxic zone, which stimulates the mobilization of sulfide from FeS, and this in turn stimulates electrogenic sulfur oxidation. The positive feedback on FeS dissolution is even more pronounced in the “reduced carbonate” simulation. Due to an absence of pH buffering by carbonates, the acidification of the suboxic zone is more intense (pH minimum = 5.1). This leads to increased FeS dissolution ( $4.6 \text{ mmol m}^{-2} \text{ d}^{-1}$  versus to  $4.2 \text{ mmol m}^{-2} \text{ d}^{-1}$  in the baseline simulation) and stronger  $\text{Fe}^{2+}$  accumulation in the pore water (0.8 mM versus 0.5 mM in the baseline). In the “reduced carbonate” simulation, iron sulfide dissolution supplies 43% of the electron donors by electrogenic sulfur oxidation.

This positive feedback process is to some extent analogous to the turbocharger principle, which make combustion engines more efficient and enables them to produce more power. This metabolic “turbo” effect is clearly seen when comparing the cathodic oxygen consumption of the baseline simulation ( $20.8 \text{ mmol m}^{-2} \text{ d}^{-1}$ ) to the simulation were FeS dissolution is purposely inhibited ( $12.5 \text{ mmol m}^{-2} \text{ d}^{-1}$ ). The metabolic dissolution of iron sulfides almost doubles

the respiration activity of the cable bacteria. It should be noted that this process is not sustainable in a steady state regime, as it depletes the sedimentary FeS pool. Recent laboratory sediment incubations have revealed that cable bacteria populations typically collapse after a period of weeks to months, and this population decline has been linked to the exhaustion of the sedimentary FeS pool (Schauer et al., 2014). Iron sulfide dissolution has been estimated to supply 94% of the sulfide for electrogenic sulfur oxidation (Risgaard-Petersen et al., 2012), and hence, the depletion of the sedimentary FeS pool would substantially reduce the electron donor supply of the cable bacteria.

Finally it should be noted that the shape of the biogeochemical fingerprint is insensitive to the sulfide source. Fig. 6 shows that even without FeS dissolution, one obtains an “electrogenic” type fingerprint that is similar in shape as when strong FeS dissolution takes place. This suggests that the shape of the geochemical fingerprint will also be robust against time-variable or non-homogeneous distributions of FeS, as could be expected under field conditions. As illustrated in Fig. 6, the emergence of an “electrogenic” type fingerprint is uniquely determined by the absence/presence of electrogenic sulfur oxidation. The geochemical depth profiles in the second column of Fig. 6 (no e-SOx simulation) differ markedly from those in the other columns. This provides further support the conclusion above that the observation of an “electrogenic” pH signature can be used as conclusive evidence for the presence of electrogenic sulfur oxidation.

#### 4.4. Cryptic sulfur cycling

Simulated sulfide concentrations are well below  $1 \mu\text{mol L}^{-1}$  within the suboxic zone, and hence, sulfide would not be detectable by  $\text{H}_2\text{S}$  micro-sensors. Still, the model reveals a strong anodic consumption of sulfide throughout the suboxic zone (Fig. 4b), which subsequently vanishes in deeper sediment layers, where sulfide first appears in the pore water. This simulation result may seem puzzling: high  $\text{H}_2\text{S}$  consumption occurs where there is no  $\text{H}_2\text{S}$  in the pore water, while no  $\text{H}_2\text{S}$  consumption occurs when there is ample  $\text{H}_2\text{S}$  in the pore water. However, this counterintuitive effect is suitably explained by the cryptic sulfur cycling that is intrinsically embedded within the model formulation.

Our sensitivity analysis shows that the cable bacteria must have a high affinity for sulfide: only for high  $k_{\text{ASO}}$  and  $k_{\text{COR}}$  values (Table 1), the model is capable of reproducing the development of a suboxic zone (Fig. 5). Due to the high affinity for sulfide, any sulfide liberated by both sulfate reduction and FeS dissolution is immediately scavenged. As a result, there is no detectable sulfide present within pore water of the suboxic zone. This cryptic sulfur cycling is further illustrated by the concave shape of the  $\text{SO}_4^{2-}$  profile within the suboxic zone, indicating that there is a net production of sulfate, and hence, sulfide must be oxidized within the suboxic zone. A similar concave sulfate profile has been demonstrated in sediment incubations with cable bacteria where FeS was the major source for electrogenic sulfide oxidation (Risgaard-Petersen et al., 2012).

Anodic sulfide consumption stops beneath the suboxic zone, as soon as sulfide starts to appear in the pore water. This observation can be explained by electron saturation of the electron chain carriers. The deeper in the sediment, the more electrons are uploaded onto the redox chain carriers by anodic sulfide consumption, and the more saturated these electron chains become (Fig. 4a). As a consequence, anodic sulfide consumption eventually becomes limited by the absence of free electron carriers (see kinetic rate expression Eq. (8)), and the sulfide which is produced by sulfate reduction starts to accumulate in the pore water, giving rise to a sharp increase of the sulfide profile at depth (Fig. 4a).

The model prediction that anodic sulfide consumption occurs throughout suboxic zone implies that cells, which are located in the suboxic zone, must be metabolically active. This suggests that cable bacteria are gaining energy and growing over the entire filament length, and not just the terminal ends that are in contact with either  $\text{O}_2$  or  $\text{H}_2\text{S}$ . This has recently been confirmed by Schauer et al. (2014), who performed detailed microscopic observations on the temporal development of the filament network, and demonstrated that cell division and filament elongation takes place throughout the suboxic zone.

#### 4.5. Carbonate dissolution

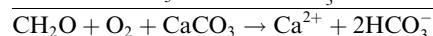
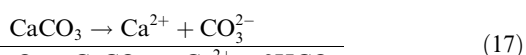
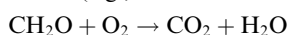
Recent studies suggest that coastal sediments could be an important source of alkalinity to the overlying water, favoring the role of the coastal ocean as a potential sink for atmospheric  $\text{CO}_2$  (Thomas et al., 2009; Faber et al., 2012). In the North Sea, it has been estimated that as much as one-quarter of the overall  $\text{CO}_2$  uptake may be driven by alkalinity production in the intertidal flat sediments of the southern North Sea (Thomas et al., 2009). In these same sediments in the North Sea, it has recently been shown that e-SOx occurs under in situ conditions in a variety of habitats, and locally exerts a large impact on the sedimentary geochemical cycling (Malkin et al., 2014). Hence, it is crucial to quantify how strongly e-SOx affects alkalinity release and calcium carbonate dissolution in coastal sediments.

Because of the spatial segregation of proton production and consumption, electrogenic sulfur oxidation generates a strong acidification at depth, while at the same time, it induces high pH values within the oxic zone. As a consequence, electrogenic sulfur oxidation strongly accelerates the dissolution of carbonates in the suboxic zone and promotes carbonate precipitation in the oxic zone (Risgaard-Petersen et al., 2012). The acidification of the suboxic zone and associated carbonate dissolution is suitably reproduced in the current model simulations. The dissolution of carbonates in the baseline simulation ( $40.9 \text{ mmol C m}^{-2} \text{ d}^{-1}$ ) is substantially higher than the release of dissolved inorganic carbon (DIC) resulting from organic matter mineralization ( $13.3 \text{ mmol C m}^{-2} \text{ d}^{-1}$ ). This implies that 75% of the DIC efflux out of the sediment is due to carbonate dissolution. As a result, one obtains a very high respiratory quotient (i.e., the ratio of DIC efflux/ $\text{O}_2$  consumption) of  $Q = 4.1$  in the baseline simulation, compared to  $Q = 1.3$  in the “No e-SOx” situation. It should be noted however that the current model simulations do not account for carbonate re-precipitation within the narrow oxic zone,

which would decrease the net carbonate dissolution in the sediment and reduce the DIC efflux across the sediment–water interface.

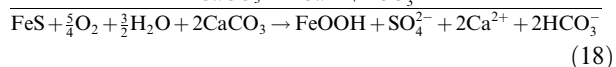
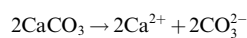
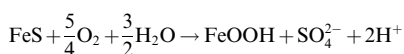
In natural sediments, carbonate re-precipitation at the surface will most likely not fully compensate for carbonate dissolution at depth. The pH maximum occurs close to the sediment water, which promotes the escape of alkalinity to the overlying water. Moreover, the pH peak within oxic zone is small (~2 mm), leading to a short transit time for solute diffusion (~30 min). As a result,  $\text{Ca}^{2+}$  and carbonate species have only a short time window in which they can react to precipitate, before escaping to the overlying water. Recent flux measurements from laboratory experiments, in which electrogenic sulfur oxidation developed in de-faunated sediment core incubations, support this idea (Rao et al., 2014). A substantial efflux of alkalinity was observed, while the DIC flux exceeded the estimated carbon mineralization rate by 25%, which hence indicates a net dissolution of carbonate in the sediment (albeit less intense than in the simulations here).

Dissolution of  $\text{CaCO}_3$  in marine sediments is principally controlled by two main mechanisms: undersaturation-driven dissolution and respiration-driven dissolution (Archer, 1996). Undersaturation-driven dissolution occurs at greater water depths (i.e., beneath the so-called carbonate saturation horizon), where the  $\text{CaCO}_3$  saturation state becomes lower than one, due to the combined effects of the biological pump and the pressure dependence of the  $\text{CaCO}_3$  solubility (Boudreau et al., 2010). In contrast, respiration-driven dissolution may occur at shallower depths where the bottom water is oversaturated with respect to calcite and aragonite. Respiration-driven dissolution is caused by the acidification of interstitial pore water by due to the respiratory activity of the benthic community, and may account for up to 50% of  $\text{CaCO}_3$  dissolution in marine sediments (Archer, 1996). Until now, respiration-driven dissolution has been primarily attributed to the release of  $\text{CO}_2$  during organic matter degradation (e.g., Hales and Emerson, 1996; Jahnke et al., 1997).



The acidifying effect of  $\text{CO}_2$  may occur either directly, as in aerobic respiration (represented by  $\text{CH}_2\text{O} + \text{O}_2 \rightarrow \text{CO}_2 + \text{H}_2\text{O}$  in (17)), or indirectly, as in anoxic respiration followed by the oxidation of reduced metabolites (the overall reaction equation would be identical to  $\text{CH}_2\text{O} + \text{O}_2 \rightarrow \text{CO}_2 + \text{H}_2\text{O}$ ).

Electrogenic sulfur oxidation induces a very different mechanism of respiration-driven carbonate dissolution, which is not dependent on organic matter mineralization, but on the proton production during the oxidation of iron sulfides. The overall effect of this form of metabolic dissolution, which is entirely independent from metabolic  $\text{CO}_2$  release, can be represented by the reaction equations:



Electrogenic sulfur oxidation could be a potentially strong driver of respiration-driven carbonate dissolution in marine sediments, thus reducing the sequestration of carbon in the form of carbonates.

## 5. CONCLUSIONS

Electrogenic sulfur oxidation (e-SOx) is a recently discovered biogeochemical process, which induces electrical currents in marine sediments, whereby electrons are transported over centimeter-scale distances from deeper anoxic sediment horizons to the sediment surface (Nielsen et al., 2010). The spatial separation of the oxidation and reduction half reactions induces strong macro-scale concentration and pH gradients in the pore water. This results in the establishment of a characteristic geochemical fingerprint (pH profile with strong excursions, wide suboxic zone), which can be accurately quantified by microsensor depth profiling. In this regard, long-distance electron transport is different from extracellular electron transport between metal-reducing bacteria and solid phase electron acceptors, where electron transport occurs at the much smaller micro-meter scale (Lovley, 2008).

Here we have developed a model description that is capable of simulating the characteristic geochemical fingerprint of e-SOx. The model is based on a conventional reactive transport description of marine sediments, which is extended with a new model formulation for long-distance electron transport. This model quantitatively supports several hypotheses about the nature of e-SOx. Firstly, our model simulations fully support the conceptual model originally proposed by Nielsen et al. (2010), in which the redox half reactions of aerobic sulfide oxidation are spatially segregated and are linked by long-distance transport. Secondly, our simulations show that electron conduction inside filamentous cable bacteria is a physically realistic mechanism to explain the observed geochemical data. This hence provides support to the proposition given by Pfeiffer et al. (2012) that cable bacteria are mediating long distance electron transport in marine sediments.

Our model analysis demonstrates that the characteristic pH profile can be used as a reliable identifier of e-SOx activity in both laboratory experiments and field studies. Sensitivity analysis showed that the characteristic geochemical fingerprint was only present when e-SOx was turned on in the model simulations. Model analysis also showed that e-SOx can strongly impact the biogeochemical cycling of C, Fe and S in marine sediments, confirming previous results from sediment incubation studies (Risgaard-Petersen et al., 2012). Due to strong acidification of the pore water, the metabolic dissolution of carbonate and metal sulfides is strongly promoted, which will ultimately reduce the burial of pyrite and carbonate in sediment environments, if these stocks are not re-supplied at some other moment in time, when the cable bacteria are not active. Finally, our model simulations suggest that cable bacteria must have a high affinity for both free sulfide and oxygen in order to create the wide suboxic zone that is observed in electro-active sediments.

The mechanistic model of long distance electron transport that is presented here envisions that the electron transport by the cable bacteria occurs by means of multistep electron hopping. Although the resulting model simulations closely reproduce the microsensor data from electro-active sediments, this does not exclude alternative mechanisms of electron transport. Future studies may investigate if there are any alternatives to multistep electron hopping that could equally well explain the presently available data. Recently, a strong debate has ignited about the nature of electron transport in nanowire pili of metal-reducing bacteria (Malvankar et al., 2012; Strycharz-Glaven and Tender, 2012). Two alternative mechanisms, multi-step electron hopping and metal-like electron transport, were put forward by different proponents, but the debate is presently unresolved. Direct measurements of the electron transport, such as current/voltage measurements on individual filaments or fiber structures of cable bacteria, would provide the most straightforward answer to the question of which conduction mechanism is underlying long-distance electron transport. However, such direct transport measurements are challenging and have not been successful so far (Pfeffer et al., 2012). Therefore, it could be worthwhile to examine as to what extent the strong imprint of electrogenic sulfur oxidation on pore water geochemistry contains any information on the physical properties of the electron conduction process.

#### ACKNOWLEDGEMENTS

The research leading to these results has received funding from the European Research Council under the European Union's Seventh Framework Programme (FP/2007-2013) through ERC Grants 306933 (FJRM) and 291650 (LPN). Furthermore, this research was financially supported by Research Foundation Flanders (Odysseus grant G.0929.08 to FJRM), Netherlands Organisation for Scientific Research (VIDI grant 864.08.004 to FJRM) the Danish National Research Foundation (DNRF104 to NR-P), and the Danish Council for Independent Research|Natural Sciences (LPN). We kindly thank the three anonymous reviewers, whose valuable suggestions and comments greatly improved this manuscript.

#### APPENDIX A.

Accordingly, the electron carriers can be in two states: uncharged (carrying no electron, denoted as  $X_j$ ) or charged (carrying an electron, denoted as  $X_j^*$ ).



Electrons can jump from one carrier to the next via bimolecular electron transfer reactions between adjacent electron carrier. This can be schematically represented by the reaction equation



where the index  $j$  denotes the position along the sequence of electron carriers separated over a distance  $\delta$ . In the context of redox polymers, this reaction mechanism is commonly referred to as “electron hopping”. The number of electrons hopping per unit of time is given by:

$$r = k(P(X_j^*)P(X_{j+1}) - \frac{1}{K_{eq}}P(X_j)P(X_{j+1}^*)) \quad (21)$$

where  $P(X_j^*)$  denotes the probability that  $j$ -th redox site is loaded with an electron. The quantity  $k$  is the kinetic rate constant of the forward reaction or hopping frequency [units:  $s^{-1}$ ], while  $K_{eq}$  is the thermodynamic equilibrium constant. If the charge carriers are all identical, as we assume here, then transition state theory requires that  $K_{eq} = 1$ .

A bacterial filament capable of long-distance electron transport hence can be idealized as a set of parallel sequences of electron carriers. If  $n_{CB}(x)$  represents the cable bacteria filament density at a given depth  $x$  in the sediment, i.e., the number of filaments that crosses a horizontal plane at that depth, and  $N_F$  denotes the number of electron conductive fibers per filament, the local density of fiber carriers becomes  $N(x) = n_{CB}(x)N_F$  [units: number of fibers  $m^{-2}$ ]. If  $\delta$  is the mean spacing between electron carriers in a conductive fiber, and  $A_F$  the cross-sectional area of a fiber, then a conductive fiber can be modelled as a set of  $A_F/\delta^2$  parallel electron carrier chains. The concentration of charge carriers at a given depth can be expressed as

$$X_T = n_{CB}(x)N_F A_F / \delta^3 \quad (22)$$

The total concentration of charge carriers can be decomposed as  $X_T = [X] + [X^*]$ , where  $[X^*]$  is the concentration of charged electron carriers and  $[X]$  is the concentration of free electron carriers. The total flux of electrons through a given depth horizon simply amounts to the electron transport within a electron carrier chain, multiplied by the number of electron carrier chains within a single fiber, multiplied with the fiber density. Thus, using Eq. (21), this flux of electrons can be calculated as

$$J(x) = n_{CB}N_F \frac{A_F}{\delta^2} k(f_C(x)f_F(x+\delta) - f_F(x)f_C(x+\delta)) \quad (23)$$

The quantity  $f_C = [X^*]/X_T$  represents the fraction of charged electron carriers, and similarly,  $f_F = [X]/X_T$  represents the corresponding fraction of free electron carriers, with

$$f_C(x) + f_F(x) = 1 \quad (24)$$

The continuum approximation and the law of large numbers allows the probabilities in Eq. (21) to be substituted in Eq. (23) with the concentration fractions. If we substitute Eq. (24) into the flux expression (23), the latter can be rearranged to (See Eq. (17) in Strycharz-Glaven et al., 2011)

$$J(x) = n_{CB}N_F \frac{A_F}{\delta^2} k \delta \left( \frac{-f_C(x+\delta) + f_C(x)}{\delta} \right) \approx - \left( n_{CB}N_F \frac{A_F}{\delta^3} \right) (k \delta^2) \frac{df_C}{dx} = -D_E X_T \frac{df_C}{dx} \quad (25)$$

Accordingly, we find that the electron transport in the parallel network of charge carriers obeys Fick's first law of diffusion. In other words, electrons tend to migrate downhill a concentration gradient of charged electron carriers. The diffusion coefficient  $D_E$  reflects the mobility of the electrons through the network and is related to the kinetic properties

of the electron hopping process (21) via the Dahms–Ruff expression

$$D_E = k\delta^2 \quad (26)$$

The above analysis assumes that the carrier network is static. If the electron carriers are also mobile and redistributed, the flux expression (25) can be generalized to:

$$J_C = -D_E X_T \nabla([X^*]/X_T) - ([X^*]/X_T) D_T \nabla X_T \quad (27)$$

$$J_F = -D_E X_T \nabla([X]/X_T) - ([X]/X_T) D_T \nabla X_T \quad (28)$$

The movement of electrons through the carrier network hence results in apparent diffusion of free (flux  $J_F$ ) and charged (flux  $J_C$ ) electron carriers. The first term on the right hand side expresses the internal transport of charges within the conducting network, while the second term reflects the bulk transport of electron carriers (where  $D_T$  is the diffusion coefficient of the electron carriers). The internal transport of charged and uncharged carriers is exactly opposite: if one charge move upwards, an “empty hole” must move downwards (analogous to the transport of electron and holes in a semi-conductor). The total flux of charged and uncharged carriers is given by

$$J_T = J_F + J_C = -D_T \nabla X_T \quad (29)$$

The diffusion coefficient  $D_T$  reflects the intensity with which the charge carriers are potentially redistributed within the sediment matrix, for example due to physical or biological reworking of the sediment. In the model simulation presented here, we do not consider such charge carrier redistribution. We assume that a network of charge carriers has been established within the sediment, which does not change with time (i.e., a fixed depth profile of  $X_T(x)$  is imposed).

## REFERENCES

- Aller R. C. (2014) Sedimentary diagenesis, depositional environments, and benthic fluxes. In *Treatise on Geochemistry*, second ed. Springer, pp. 293–334.
- Aller R. C. and Rude P. D. (1988) Complete oxidation of solid phase sulfides by manganese and bacteria in anoxic marine sediments. *Geochim. Cosmochim. Acta* **52**, 751–765.
- Andrieux C. P. and Saveant J. M. (1980) Electron transfer through redox polymer films. *J. Electroanal. Chem.* **111**, 377–381.
- Archer D. E. (1996) A data-driven model of the global calcite lysocline. *Global Biogeochem. Cycles* **10**, 511–526.
- Berg P., Rysgaard S. and Thamdrup B. (2003) Dynamic modeling of early diagenesis and nutrient cycling: A case study in an Arctic marine sediment. *Am. J. Sci.* **303**, 905–955.
- Boudreau B. P. (1996a) A method-of-lines code for carbon and nutrient diagenesis in aquatic sediments. *Comput. Geosci.* **22**, 479–496.
- Boudreau B. P. (1996b) The diffusive tortuosity of fine-grained un lithified sediments. *Geochim. Cosmochim. Acta* **60**, 3139–3142.
- Boudreau B. P. (1997) *Diagenetic Models and Their Implementation*. Springer.
- Boudreau B. P., Middelburg J. J. and Meysman F. J. R. (2010) Carbonate compensation dynamics. *Geophys. Res. Lett.* **37**. <http://dx.doi.org/10.1029/2009GL041847>.
- Canfield D. E., Jorgensen B. B., Fossing H., Glud R., Gundersen J., Ramsing N. B., Thamdrup B., Hansen J. W., Nielsen L. P. and Hall P. O. J. (1993) Pathways of organic carbon oxidation in 3 continental margin sediments. *Mar. Geol.* **113**, 27–40.
- Canfield D. E., Kristensen E. and Thamdrup B. (2005) Aquatic geomicrobiology. *Adv. Mar. Biol.* **48**, 1–599.
- Clarke T. A., Edwards M. J., Gates A. J., Hall A., White G. F., Bradley J., Reardon C. L., Shi L., Beliaev A. S., Marshall M. J., Wang Z., Watmough N. J., Fredrickson J. K., Zachara J. M., Butt J. N. and Richardson D. J. (2011) Structure of a bacterial cell surface decaheme electron conduit. *Proc. Nat. Acad. Sci. U.S.A.* **108**, 9384–9389.
- Dalton E. F., Surridge N. A., Jernigan J. C., Wilbourn K. O., Facci J. S. and Murray R. W. (1990) Charge transport in electroactive polymers consisting of fixed molecular redox sites. *Chem. Phys.* **141**, 143–157.
- Damgaard L. R., Risgaard-Petersen N. and Nielsen L. P. (2014) Electric Potential microelectrode for studies of electrobiogeophysics. *J. Geophys. Res. Biogeosciences* **119**(9), 1906–1917.
- Davison W., Phillips N. and Tabner B. J. (1999) Soluble iron sulfide species in natural waters: Reappraisal of their stoichiometry and stability constants. *Aquat. Sci.* **61**, 23–43.
- El-Naggar M. Y., Wanger G., Leung K. M., Yuzvinsky T. D., Southam G., Yang J., Lau W. M., Neelson K. H. and Gorby Y. A. (2010) Electrical transport along bacterial nanowires from *Shewanella oneidensis* MR-1. *Proc. Nat. Acad. Sci. U.S.A.* **107**, 18127–18131.
- Faber P., Kessler A., Bull J., McKelvie I., Meysman F. and Cook P. (2012) The role of alkalinity generation in controlling the fluxes of CO<sub>2</sub> during exposure and inundation on tidal flats. *Biogeosciences* **9**, 4087–4097.
- Froelich P. N., Klinckhammer G. P., Bender M. L., Luedtke N. A., Heath G. R., Cullen D., Dauphin P., Hammond D. E., Hartman B. and Maynard V. (1979) Early oxidation of organic matter in pelagic sediments of the eastern equatorial Atlantic: Suboxic diagenesis. *Geochim. Cosmochim. Acta* **43**, 1075–1090.
- Glud R. N. (2008) Oxygen dynamics of marine sediments. *Mar. Biol. Res.* **4**, 243–289.
- Gorby Y. A., Yanina S., McLean J. S., Rosso K. M., Moyles D., Dohnalkova A., Beveridge T. J., Chang I. S., Kim B. H., Kim K. S., Culley D. E., Reed S. B., Romine M. F., Saffarini D. A., Hill E. A., Shi L., Elias D. A., Kennedy D. W., Pinchuk G., Watanabe K., Ishii S. I., Logan B., Neelson K. H. and Fredrickson J. K. (2006) Electrically conductive bacterial nanowires produced by *Shewanella oneidensis* strain MR-1 and other microorganisms. *Proc. Nat. Acad. Sci. U.S.A.* **103**, 11358–11363.
- Gray H. B. and Winkler J. R. (2005) Long-range electron transfer. *Proc. Nat. Acad. Sci. U.S.A.* **102**, 3534–3539.
- Hales B. and Emerson S. (1996) Calcite dissolution in sediments of the Ontong-Java Plateau: In situ measurements of pore water O<sub>2</sub> and pH. *Glob. Biogeochem. Cycl.* **10**, 527–541.
- Hofmann A. F., Meysman F. J. R., Soetaert K. and Middelburg J. J. (2008) A step-by-step procedure for pH model construction in aquatic systems. *Biogeosciences* **5**, 227–251.
- Hofmann A. F., Soetaert K., Middelburg J. J. and Meysman F. J. R. (2010) AquaEnv: An Aquatic Acid-Base Modelling Environment in R. *Aquat. Geochem.* **16**, 507–546.
- Jahnke R. A., Craven D. B., McCorckle D. C. and Reimers C. E. (1997) CaCO<sub>3</sub> dissolution in California continental margin sediments: The influence of organic matter mineralization. *Geochim. Cosmochim. Acta* **61**, 3587–3604.
- Jorgensen B. B. (1977) Sulfur cycle of a coastal marine sediment (Limfjorden, Denmark). *Limnol. Oceanogr.* **22**, 814–832.
- Jorgensen B. B. (1982) Mineralization of organic matter in the seabed – The role of sulfate reduction. *Nature* **296**, 643–645.

- Jorgensen B. B. and Revsbech N. P. (1983) Colorless sulfur bacteria *Beggiatoa* and *Thiovulum* spp. in O<sub>2</sub> and H<sub>2</sub>S microgradients. *App. Environ. Microbiol.* **45**, 1261–1270.
- Jourabchi P., Van Cappellen P. and Regnier P. (2005) Quantitative interpretation of pH distributions in aquatic sediments: A reaction-transport modelling approach. *Am. J. Sci.* **305**, 919–956.
- Kato S., Nakamura R., Kai F., Watanabe K. and Hashimoto K. (2010) Respiratory interactions of soil bacteria with (semi)conductive iron-oxide minerals. *Environ. Microbiol.* **12**, 3114–3123.
- Logan B. E. and Rabaey K. (2012) Conversion of wastes into bioelectricity and chemicals by using microbial electrochemical technologies. *Science* **337**, 686–690.
- Lovley D. R. (2008) Extracellular electron transfer: Wires, capacitors, iron lungs, and more. *Geobiology* **6**, 225–231.
- Malkin S. Y., Rao A. M. F., Seitaj D., Vasquez-Cardenas D., Zetsche E., Boschker H. T. S. and Meysman F. J. R. (2014) Natural occurrence of microbial sulfur oxidation by long-range electron transport in the seafloor. *ISME J.* <http://dx.doi.org/10.1038/ismej.2014.41>.
- Malvankar N. S., Tuominen M. T. and Lovley D. R. (2012). *Energy Environ. Sci.* **5**, 6247–6249.
- Malvankar N. S., King G. and Lovley D. R. (2014) Centimeter-long electron transport in marine sediments via conductive minerals. *ISME J.* <http://dx.doi.org/10.1038/ismej.2014.131>.
- Meysman F. J. R., Boudreau B. P. and Middelburg J. J. (2005) Modeling reactive transport in sediments subject to bioturbation and compaction. *Geochim. Cosmochim. Acta* **69**, 3601–3617.
- Meysman F. J. R., Middelburg J. J., Herman P. M. J. and Heip C. H. R. (2003) Reactive transport in surface sediments. II. Media: An object-oriented problem-solving environment for early diagenesis. *Comput. Geosci.* **29**, 301–318.
- Millero F. J., Graham T. B., Huang F., Bustos-Serrano H. and Pierrot D. (2006) Dissociation constants of carbonic acid in seawater as a function of salinity and temperature. *Mar. Chem.* **100**, 80–94.
- Munhoven G. (2013) Mathematics of the total alkalinity pH equation – Pathway to robust and universal solution algorithms: The SolveSAPHE package v1.0.1. *Geosci. Mod. Dev.* **6**, 1367–1388.
- Nealson K. H. (2010) Sediment reactions defy dogma. *Nature* **463**, 1033–1034.
- Nielsen L. P., Risgaard-Petersen N., Fossing H., Christensen P. B. and Sayama M. (2010) Electric currents couple spatially separated biogeochemical processes in marine sediment. *Nature* **463**, 1071–1074.
- Ntarlagiannis D., Atekwana E. A., Hill E. A. and Gorby Y. (2007) Microbial nanowires: Is the subsurface “hardwired”? *Geophys. Res. Lett.* **34**. <http://dx.doi.org/10.1029/2007GL030426>.
- Pfeffer C., Larsen S., Song J., Dong M., Besenbacher F., Meyer R. L., Kjeldsen K. U., Schreiber L., Gorby Y. A., El-Naggar M. Y., Leung K. M., Schramm A., Risgaard-Petersen N. and Nielsen L. P. (2012) Filamentous bacteria transport electrons over centimetre distances *Nature* **491**, 218–221.
- Pokkuluri P. R., Londer Y. Y., Duke N. E. C., Pessanha M., Yang X., Orshonsky V., Orshonsky L., Erickson J., Zagayanskiy Y., Salgueiro C. A. and Schiffer M. (2011) Structure of a novel dodecaheme cytochrome *c* from *Geobacter sulfurreducens* reveals an extended 12 nm protein with interacting hemes. *J. Struct. Biol.* **174**, 223–233.
- Polizzi N. F., Skourtis S. S. and Beratan D. N. (2012) Physical constraints on charge transport through bacterial nanowires. *Faraday Discuss.* **155**, 43–62.
- Rao A. M. F., Malkin S. Y., Montserrat F. and Meysman F. J. R. (2014) Alkalinity production in intertidal sands intensified by lugworm bioirrigation. *Estuar. Coast. Shelf Sci.* **148**, 36–47.
- Reguera G., McCarthy K. D., Mehta T., Nicoll J. S., Tuominen M. T. and Lovley D. R. (2005) Extracellular electron transfer via microbial nanowires. *Nature* **435**, 1098–1101.
- Rickard D. (2006) The solubility of FeS. *Geochim. Cosmochim. Acta* **70**, 5779–5789.
- Risgaard-Petersen N., Revil A., Meister P. and Nielsen L. P. (2012) Sulfur, iron-, and calcium cycling associated with natural electric currents running through marine sediment. *Geochim. Cosmochim. Acta* **92**, 1–13.
- Risgaard-Petersen N., Damgaard L. R., Revil A. and Nielsen L. P. (2014) Mapping electron sources and sinks in a marine biogeobattery. *J. Geophys. Res. Biogeosciences* **119**, 1475–1486.
- Sayama M., Risgaard-Petersen N., Nielsen L. P., Fossing H. and Christensen P. B. (2005) Impact of bacterial NO<sub>3</sub><sup>-</sup> transport on sediment biogeochemistry. *App. Environ. Microbiol.* **71**, 7575–7577.
- Schauer R., Risgaard-Petersen N., Kjeldsen K. U., Tataru Bjerg J. J., Jorgensen B. B., Schramm A. and Nielsen L. P. (2014) Succession of cable bacteria and electric currents in marine sediment. *ISME J.* **8**, 1314–1322.
- Soetaert K., Herman P. M. J. and Middelburg J. J. (1996) A model of early diagenetic processes from the shelf to abyssal depths. *Geochim. Cosmochim. Acta* **60**, 1019–1040.
- Soetaert K., Hofmann A. F., Middelburg J. J., Meysman F. J. R. and Greenwood J. (2007) The effect of biogeochemical processes on pH. *Mar. Chem.* **105**, 30–51.
- Soetaert K. and Meysman F. (2012) Reactive transport in aquatic ecosystems: Rapid model prototyping in the open source software R. *Environ. Mod. Soft.* **32**, 49–60.
- Soetaert K., Petzoldt T. and Setzer R. W. (2010) Solving differential equations in R. *R Journal* **2**, 5–15.
- Strycharz-Glaven S. M., Snider R. M., Guiseppi-Elie A. and Tender L. M. (2011) On the electrical conductivity of microbial nanowires and biofilms. *Energy Environ. Sci.* **4**, 4366–4379.
- Strycharz-Glaven S. M. and Tender L. M. (2012). *Energy Environ. Sci.* **5**, 2650–2655.
- Thomas H., Schiettecatte L.-S., Suykens K., Koné Y., Shadwick E., Prowe A., Bozec Y., de Baar H. and Borges A. (2009) Enhanced ocean carbon storage from anaerobic alkalinity generation in coastal sediments. *Biogeosciences* **6**, 267–274.
- Van Cappellen P. and Wang Y. F. (1996) Cycling of iron and manganese in surface sediments: A general theory for the coupled transport and reaction of carbon, oxygen, nitrogen, sulfur, iron, and manganese. *Am. J. Sci.* **296**, 197–243.

Associate editor: Josef P. Werne